Systematic uncertainties in shock-wave impedance-match analysis and the high-pressure equation of state of Al

P. M. Celliers,[a] G. W. Collins, D. G. Hicks, and J. H. Eggert
Lawrence Livermore National Laboratory, Livermore, California 94550

A method for producing quantitative estimates of systematic uncertainties generated in the analysis of impedance-match shock-wave data is described. Central to the method is an analytic representation of the principal Hugoniot of the standard which incorporates a description of data-dependent uncertainties of the principal Hugoniot and model-dependent uncertainties of the off-Hugoniot states. Expressions for the sound speed and Grüneisen coefficient along the principal Hugoniot are also derived with uncertainties. An accurate impedance-match shock-wave equation of state for Al to shock pressure of 3 TPa is given and is used to estimate the systematic uncertainties of several previously published experimental results. © *2005 American Institute of Physics*. [DOI: 10.1063/1.2140077]

I. INTRODUCTION

Shock-wave impedance-match measurements are a common method of producing shock-wave equation-of-state (EOS) data for a variety of different sample materials. These measurements are performed by transmitting a shock wave from a known material (the reference standard) into an unknown sample.[1–4] From measurements of two observables, usually the shock velocities in the standard and in the sample, and using the Rankine-Hugoniot conservation relations, one can deduce the pressure, density, and internal energy in the shocked sample. Such measurements depend on the accurate knowledge of the equation of state of the standard and are therefore considered as *relative* measurements. The shock-wave EOS of the standard must be calibrated, usually through a series of separate *absolute* measurements. The data from absolute measurements are independent of the theoretical or model-dependent input, and the uncertainties in the EOS of the standard can be traced to measurement uncertainties. In the case of relative measurements, the uncertainties in the EOS of the standard propagate as *systematic* errors because the data must be reduced using imperfect knowledge of the EOS of the standard.

The impedance-match method is important because it is the simplest, and sometimes the only, means available to obtain shock-wave data on some types of samples, for example, fluid samples[5–8] or in the ultrahigh ranges of shock pressure.[9–11] In recent years impedance-match techniques have been applied to obtain shock-wave EOS data at ever higher pressures in laboratory experiments using, for example, laser-driven shock waves,[8,12–14] magnetically driven flyer plates,[15] or convergent explosive systems.[16–18] In the latter cases, the experiments have reached a pressure domain where experimental knowledge of the EOS of the standard is sparse. A further complication with impedance-match analysis is that, except at the lowest pressures, one cannot avoid introducing theoretical (i.e., model dependent) input in the calculations. In particular, most of the recent studies that we are aware of employ theoretical EOS models to perform the impedance-match analysis.[8–18] Because of the difficulties of separating out and assessing the systematic bias contained in a given theoretical EOS model, these studies estimated the random (measurement) errors but not the systematic uncertainties. Since the accuracy of the impedance-match method is related to the accuracy of our knowledge of the standard and of the systematic details of the impedance-match analysis itself, it is important to produce quantitative estimates of the systematic uncertainties in the analyzed results.

In this article we describe a method for impedance-match analysis that addresses the issues described above. It quantifies the uncertainties of both the random measurement and systematic error contributions. In developing this method we have focused on the aluminum shock-wave standard because it is one of the most common standards available and is used frequently in our own experiments. We apply the analysis to the data available from several recent experiments. Knowledge of the systematic uncertainties together with the random measurement uncertainties allows a comprehensive assessment of the overall accuracy of the resulting data.

II. IMPEDANCE-MATCH ANALYSIS

A. Outline of impedance-match calculations

In impedance-match equation-of-state experiments the reference and sample impedances generally do not match, and the incident shock wave resolves into a transmitted shock and a reflected wave directed back into the standard material. When the sample impedance is lower than that of the standard, the reflected wave is a rarefaction, and the standard undergoes an isentropic release; when the sample impedance is higher the reflected wave is a shock, and the standard undergoes further shock compression.

[a] Electronic mail: celliers1@llnl.gov
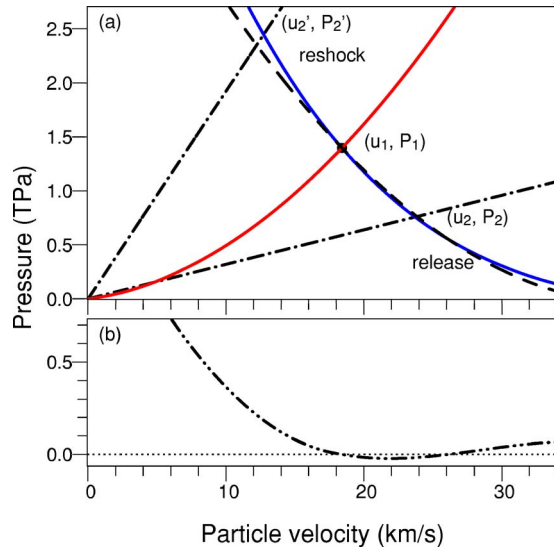
98, 113529-1

FIG. 1. (Color online) (a) Graphical representation of impedance-match analysis for an incident shock of 1.4 TPa in Al. The solid (red) curve with positive slope is the principal Hugoniot of the Al standard, and the incident shock state is indicated by the filled circle at (u_1, P_1). A low-impedance sample is represented by the lower dash-dot line and the impedance-match state (u_2, P_2) while a high-impedance sample produces a reflected shock and the state (u_2', P_2'). The solid (blue) curve of negative slope shows locus of states accessed by the reflected shock and release states, $P_{R_1}(u)$, passing through (u_1, P_1); the dashed (black) curve of negative slope shows the mirror reflection of the principal Hugoniot $P_{M_1}(u)$. (b) The pressure correction P_{C_1} (dash-dot curve) shows the difference $P_{R_1} - P_{M_1}$, corresponding to the Hugoniot states above.

The shock incident in the standard and that transmitted into the sample both obey the Rankine-Hugoniot relations, which express the conservation of mass, momentum, and energy across the shock front,

$$\frac{\rho_i}{\rho_{i0}} = \frac{U_i}{U_i - u_i}, \tag{1}$$

$$P_i - P_{i0} = \rho_{i0} u_i U_i, \tag{2}$$

$$E_i - E_{i0} = \frac{1}{2}(P_i + P_{i0})\left(\frac{1}{\rho_{i0}} - \frac{1}{\rho_i}\right). \tag{3}$$

In the following we use the subscript $i=1$ to denote the incident (first) shock state in the standard and $i=2$ to denote the state of the shock transmitted into the sample; $i0$ denotes initial states. The pressure P, density ρ, and internal energy E are the thermodynamic variables, and U and u are the shock velocity and fluid velocity behind the shock front, respectively. By measuring two observables and combining these with Eqs. (1)–(3), the remaining parameters can be determined. This determination is obtained because conservation of mass and momentum is maintained at the interface between the standard and the sample upon the passage of the shock front through it, so that the sample and standard maintain a common pressure and fluid velocity at the interface between them. Once these quantities are known the Rankine-Hugoniot relations can be applied to determine ρ and E in the sample.

To determine the common P_2 and u_2 at the standard-sample interface, calculations are generally carried out on the

P-u plane,[1,2] as shown in Fig. 1(a). The state (u_1, P_1) lies on the known principal Hugoniot of the standard. The unknown state in the sample (u_2, P_2) lies along a straight line of slope $\rho_{20} U_2$ passing through the origin of the P-u plane ($P_{20}=0$ in most cases), following the relation given by Eq. (2). The states (u_1, P_1) in the standard and (u_2, P_2) in the sample are connected by the reflected wave in the standard; this connection follows a curve that originates from the state along the principal Hugoniot and moves *off* the Hugoniot. The branch of this curve reaching higher pressures follows a second shock Hugoniot, centered on the state ρ_1, P_1, and E_1, and can be expressed by an equation of the form

$$P_{R1}(u) = P_1 + \rho_1 |u - u_1| \hat{U}(|u - u_1|), \quad u < u_1, \tag{4}$$

which expresses Eq. (2) for the reflected shock in the standard; $\hat{U}(u)$ gives the dependence of shock velocity as a function of fluid velocity behind the (second) reflected shock. The branch reaching to lower pressures follows an isentropic release and can be found by computing the integral,

$$u = u_1 - \int_{P_1}^{P_2} \frac{dP}{\rho_{R1} c_{R1}}, \quad P_2 < P_1, \tag{5}$$

where ρ_{R1} and c_{R1} are the density and isentropic sound velocity, respectively, in the standard evaluated along an integration path that follows the thermodynamic isentrope passing through the state (ρ_1, P_1, E_1). In either case, these curves cannot be computed accurately without knowledge of the equation of state of the standard both on and off the principal Hugoniot. In most situations only limited knowledge of the off-Hugoniot states in the standard is available, and therefore model-dependent input is required to determine the reshock and release profiles.

B. Systematic effects

Systematic effects enter through the fact that uncertainties are associated with the principal Hugoniot and with the off-Hugoniot curves used to construct the solution in Fig. 1(a). Depending on the method of analysis, there may also exist a systematic *bias* either because the model used for the analysis may misfit the available data in a systematic way (e.g., may represent the reference EOS either on the soft or the stiff side of the available data) or because the method used to evaluate the off-Hugoniot curves may contain approximations. Both the systematic uncertainty and bias tend to cause a general shift the analyzed the data as a group (e.g., to be more or less compressible depending on whether a soft or stiff bias is present in the model for the standard).

For the off-Hugoniot states a well-known practical approximation is a graphical construction which approximates the reshock and release profiles by the mirror reflection of the principal Hugoniot in the P-u plane about the point along the Hugoniot corresponding to the incident shock state in the reference standard.[1,2] For sample materials with similar impedance to that of the standard, or at low pressures (<0.2 TPa), this construction allows for remarkably accurate results, but the accuracy diminishes for greater mismatch of the impedances and with high (>0.2 TPa) incident shock pressure. The advantage of the mirror-reflected Hugoniot ap-

proximation is that the uncertainty in the principal Hugoniot can be propagated into the mirror-reflection construction with standard methods. However, especially at high pressures, the mirror-reflection approximation differs systematically from the exact reshock and release curves,[19] as indicated Fig. 1(a); therefore its use will impose a systematic bias. The accuracy of this approximation has been examined experimentally[20,21] and theoretically[22] for release states in several materials. The latter study estimated, based on theoretical models, that the range of validity for the use of the mirror-reflection approximation requires $u_2/u_1 - 1 < 0.6$ in order that the systematic errors $\delta u_{2sys}/u_2 < 1\% - 1.5\%$ in determining u_2 for low-impedance samples. This limit restricts the analysis to sample densities $\rho_{20} > 0.6$ g cm^{-3} in the case of an Al reference standard.

The obvious solution to this situation is to apply a correction, as suggested by Fig. 1(b). For example, expressions for reshock and release states using the Mie-Grüneisen model have been worked out by McQueen *et al.*;[23] along these lines Nellis and co-workers have applied such a correction in the analysis of impedance-match data of shock-compressed fluids.[5,24] However, for applications over a wide range of states, the common Grüneisen approximations such as $\Gamma/V = \text{const}$ are not general enough; for example, in the high-pressure domain $\Gamma \sim 0.4 \sim \text{const}$ for a wide range of materials.[25] Our aim is to construct a correction valid over a wide range ($0.1 < P < 3$ TPa), where thermal electronic and ionic contributions to the pressure become dominant.

Because of the issues outlined above, the recent studies[8–18] that we are aware of avoid the mirror-reflected Hugoniot approximation and instead use theoretical EOS models (different authors use different models) both to represent the principal Hugoniot of the standard and to compute the accurate off-Hugoniot states. By construction the EOS model is usually fit to a subset of the available data for the standard and contains rigorous theoretical content to represent the reshock and release profiles accurately. This provides a significant advantage but comes at the expense of eliminating any representation of the uncertainties in the underlying Hugoniot data or uncertainties in the parameters used to construct the model. In the widely used SESAME library[26] there exist several theoretical EOS models for aluminum; these were constructed for a variety of reasons, with varying levels of theoretical rigor and with varying qualities of fit to the available data. When used for impedance-match analysis all produce somewhat different results.

III. IMPEDANCE-MATCH ANALYSIS INCLUDING SYSTEMATIC EFFECTS

In this section we present a method for performing impedance-match EOS data reduction and error propagation that addresses the issues raised above. Following the approaches outlined earlier by Nellis and Mitchell,[5] we combine (i) the measured principal Hugoniot of the standard, as given by a fit to the available absolute (i.e., model independent) data and (ii) an additional polynomial, as suggested in

Fig. 1(b), that corrects the mirror-reflection approximation to produce an accurate representation of the off-Hugoniot states (reshock and release).

As outlined in Sec. II A, calculations take place in the P-u plane, for which u is viewed as the independent variable and P as the dependent variable. The principal Hugoniot of the standard is represented by the function $U(u)$, giving the shock velocity U as a function of particle velocity u along the Hugoniot. The pressure along the principal Hugoniot is given by

$$P_H(u) = \rho_{10} u U(u) \tag{6}$$

(from Eq. (1)). From a measurement of the shock state in the standard, the fluid velocity behind the shock, u_1, can be determined, and the mirror-reflected Hugoniot can be defined,

$$P_{M_1}(u) = P_H(2u_1 - u) = \rho_{10}(2u_1 - u)U(2u_1 - u). \tag{7}$$

Accurate reshock and release profiles $P_{R_1}(u)$ are then produced by correcting the mirror-reflected curve with a model-dependent pressure correction $P_{C_1}(u)$, that is,

$$P_{R_1}(u) = P_{M1}(u) + P_{C_1}(u), \tag{8}$$

where the subscript 1 indicates an explicit dependence of these functions on the incident state, parametrized by u_1. As noted above, the pressure correction is necessary to remove the systematic bias of the mirror-reflected Hugoniot approximation over a wide range of pressures (i.e., samples with much higher or lower impedance than the standard).

The second observable in an experiment is the measured shock velocity of the shock transmitted into the sample, U_2. Using this variable the impedance-match solution is found by solving the equation $P_{R_1}(u) - \rho_{20} u U_2 = 0$ for u, or more explicitly,

$$\rho_{10}(2u_1 - u)U(2u_1 - u) + P_{C_1}(u) - \rho_{20} u U_2 = 0; \tag{9}$$

the solution yields the value u_2, which then yields P_2, ρ_2, and E_2 through Eqs. (1)–(3).

The two main functions in the analysis, $U(u)$ and $P_{C_1}(u)$, are constructed through fitting procedures. The available Hugoniot data define $U(u)$ and therefore $P_H(u)$ and $P_{M_1}(u)$. The correction P_{C_1} is estimated from an average over several theoretical models. The fitting procedures allow us to determine systematic uncertainties: The standard deviation in the fit to $U(u)$ gives the function $\sigma_U(u)$ and the standard deviation of $P_{C_1}(u)$ derived from an ensemble of theoretical models gives the function $\sigma_{P_{C_1}}(u)$. These additional functions can be introduced into Eq. (9) in order to propagate the systematic uncertainties. In the sections below we give explicit definitions for all of these functions.

For both $U(u)$ and $P_{C_1}(u)$ the fits employ orthogonal polynomials with coefficients a_i and b_i, respectively, that

have been assigned with uncertainties σ_{a_i} and σ_{b_i} determined through the fitting procedures. Orthogonal polynomial constructions are employed so that the error contributions for each coefficient are easily evaluated and combined in quadrature to produce a total evaluation for the uncertainties,

$$\sigma_U = \left[\sum_j \sigma_{a_j}^2 \left(\frac{\partial U}{\partial a_j} \right)^2 \right]^{1/2} \quad \text{and} \tag{10}$$

$$\sigma_{P_{C_1}} = \left[\sum_j \sigma_{b_j}^2 \left(\frac{\partial P_{C_1}}{\partial b_j} \right)^2 \right]^{1/2}.$$

A. Fit to the principal Hugoniot

The primary means of representing the principal Hugoniot of a shock-wave reference standard is through the relationship between shock speed and particle speed. For most cases this relationship has been demonstrated to be linear (sometimes with small quadratic corrections) over large ranges of these variables and is typically represented by the equation

$$U = C + Su + Tu^2, \tag{11}$$

where U is the shock velocity, u is the fluid velocity behind the shock, and C, S, and T are the fitting parameters. Standard deviation uncertainties for the fitting parameters are usually given when the Hugoniot results are reported. These standard deviations are given by standard error analysis expressions, for example, in the case of σ_C,

$$\sigma_C = \left[\sum_j \sigma_j^2 \left(\frac{\partial C}{\partial U_j} \right)^2 \right]^{1/2}, \tag{12}$$

where σ_j is the standard deviation of the jth datum in the data set used for the fit (more details are given in the Appendix). For propagating the error in an impedance-match analysis, the relevant quantity is the estimated standard deviation of the shock velocity, $\sigma_U(u)$, as a function of the given particle velocity u. Although it is common to supply uncertainties ($\pm \delta C$, $\pm \delta S$, and $\pm \delta T$) when such fits are reported in the literature, we note that these uncertainties provide incomplete information, because σ_U cannot be derived solely from the uncertainties in the fit parameters. Specifically,

$$\sigma_U(u) = \left[\sum_j \sigma_j^2 \left(\frac{\partial C}{\partial U_j} + u \frac{\partial S}{\partial U_j} + u^2 \frac{\partial T}{\partial U_j} \right)^2 \right]^{1/2}. \tag{13}$$

Explicit evaluation of this expression involves summations over cross terms, e.g., $\sum_j \sigma_j^2 u^2 (\partial C / \partial U_j)(\partial S / \partial U_j)$, which involve covariances between the coefficients of the fit. This was recognized by Mitchell and Nellis;[27] these authors supplied an additional set of coefficients that defined a quadratic fit to $2\sigma_U$.

To simplify this situation we use an orthogonal polynomial basis, constructed such that the covariances among the fitting coefficients vanish; therefore, for the purpose of error

propagation, the coefficients are independent. Using the orthogonal polynomial basis, we represent the fit to the Hugoniot data with the following expression:

$$U(u) = a_0 + a_1(u - \beta) + a_2(u - \gamma_1)(u - \gamma_2), \tag{14}$$

where the parameters a_i are the coefficients of the fit and β, γ_1, and γ_2 are the parameters of the orthogonal basis. The fitting process also determines the standard deviations σ_{a_i} for each of the coefficients. The standard deviation in the fit, σ_U, is represented in terms of the standard deviations of the coefficients,

$$\sigma_U(u) = [\sigma_{a_0}^2 + \sigma_{a_1}^2(u - \beta)^2 + \sigma_{a_2}^2(u - \gamma_1)^2(u - \gamma_2)^2]^{1/2}. \tag{15}$$

The Appendix gives an explicit procedure for generating these parameters from a primary Hugoniot data set.

B. Off-Hugoniot correction

The off-Hugoniot correction is defined in terms of normalized variables,

$$P_{C_1}(u) = P_H(u_1) p_{n_1}(u/u_1 - 1), \tag{16}$$

where $p_{n_1}(q)$ is the pressure correction normalized against the Hugoniot pressure $P_H(u_1)$ of the incident shock in the standard, and the variable $q = u/u_1 - 1$ is a normalized particle velocity with the origin shifted such that the two branches of the pressure correction are centered at $q=0$. For reflected shocks (reshocks), $q<0$, and for release waves $q>0$. The particle velocity u_1 is determined from the inverse relation $u_1 = U^{-1}(U_1)$.

The pressure correction is expanded in a series of the Chebyshev polynomials and given by an expression defined as follows:

$$p_{n_1}(q)$$
$$= \begin{cases} \displaystyle\sum_{i=1}^{2} b_{si}(u_1)[T_i(3q+1) - 1] & \text{for } -2/3 < q \leqslant 0 \\ \displaystyle\sum_{i=1}^{3} b_{ri}(u_1)[T_i(2q-1) - (-1)^i] & \text{for } 0 < q \leqslant 1, \end{cases} \tag{17}$$

where T_i are the Chebyshev polynomials[28] of order i. The coefficients $b_{si}(u_1)$ and $b_{ri}(u_1)$ and their respective uncertainties depend on the particle velocity u_1 and are determined through fitting procedures as described in the Appendix.

As with the expression for $\sigma_U(u)$, the standard deviation of the pressure correction depends on the uncertainties in the fitting coefficients. By construction the Chebyshev polynomials are orthogonal over the domain of the fit, and the individual coefficient uncertainties can be combined in a quadrature form, as indicated in Eq. (10), leading to the expression

$$\sigma_{p_{n_1}}(q) = \begin{cases} \left[\sum_{i=1}^{2} \sigma_{b_{si}}(u_1)^2 [T_i(3q+1)-1]^2 \right]^{1/2} & \text{for } -2/3 < q \leq 0 \\ \left[\sum_{i=1}^{3} \sigma_{b_{ri}}(u_1)^2 [T_i(2q-1)-(-1)^i]^2 \right]^{1/2} & \text{for } 0 < q \leq 1. \end{cases} \tag{18}$$

The uncertainty in the pressure correction as a function of the particle velocity is

$$\sigma_{P_{C_1}}(u) = P_H(u_1)\sigma_{p_{n_1}}(u/u_1 - 1). \tag{19}$$

The Appendix describes in detail the method for generating the fitting coefficients and their uncertainties from a set of theoretical models.

C. Implementation for impedance-match analysis

In order to propagate systematic errors, the functions $U(u)$ and $P_{C_1}(u)$ have to be combined with their respective uncertainties, $\sigma_U(u)$ and $\sigma_{P_{C_1}}(u)$. For that purpose we introduce modified versions of the functions introduced above,

$$U^*(u;\lambda) = U(u) + \lambda\sigma_U(u), \tag{20}$$

$$P_H^*(u;\lambda) = \rho_{10}u U^*(u;\lambda), \tag{21}$$

$$P_{C_1}^*(u,u_1;\lambda,\epsilon) = P_H^*(u_1;\lambda)[p_{n_1}(u/u_1 - 1) + \epsilon\sigma_{p_{n_1}}(u/u_1 - 1)]. \tag{22}$$

Here the parameters λ and ϵ introduce systematic variations to the impedance-match curves measured in units of the standard deviations. For example $U^*(u;1)$ represents a U-u Hugoniot curve that is offset systematically on the stiff side by one standard deviation from the best-fit curve.

The propagation of systematic errors differs depending on whether the shock state in the standard is determined by observing the shock velocity U_1 (laser-driven shock or nuclear impedance-match experiments) or the particle velocity u_1 (for example, by symmetric impact of a flyer plate whose velocity is known). The two cases are treated separately in the following sections.

1. Analysis with U_1 observable

For measurements in this class the primary observables (with random errors) are $U_1 \pm \delta U_1$ and $U_2 \pm \delta U_2$, the shock velocities in the standard and sample, respectively. In this situation there is a systematic uncertainty in the value of u_1 arising from the uncertainty in the EOS. Consequently, both the pressure P_1 and the particle velocity u_1 of the launch point for the reshock or release profiles vary with a variation in the EOS of the standard. At this point we also introduce the parameters ξ and ζ to propagate the random errors. Taking these into account we introduce the variable $u_{1\lambda\xi}^*$, which depends on λ, ξ, U_1, and δU_1, and is found by solving the

equation $U^*(u_{1\lambda\xi}^*;\lambda) = U_1 + \xi\delta U_1$. The impedance-match solution equation (9) modified to include systematic and random variations is then given by

$$\rho_{10}[2u_{1\lambda\xi}^* - u]U^*(2u_{1\lambda\xi}^* - u;\lambda) + P_{C_1}^*(u,u_{1\lambda\xi}^*;\lambda,\epsilon) - \rho_{20}u[U_2 + \zeta\delta U_2] = 0. \tag{23}$$

Solution of this equation for u yields $u_2(\lambda,\epsilon,\xi,\zeta)$, and the Rankine-Hugoniot relation equations [(1)–(3)] are then used to determine $P_2(\lambda,\epsilon,\xi,\zeta)$, $\rho_2(\lambda,\epsilon,\xi,\zeta)$, and $E_2(\lambda,\epsilon,\xi,\zeta)$.

The nominal (neutrally biased) solution is found initially for $\epsilon = \lambda = \xi = \zeta = 0$. A series partial derivatives,

$$\frac{\partial u_2}{\partial\lambda}, \frac{\partial u_2}{\partial\epsilon}, \frac{\partial P_2}{\partial\lambda}, \frac{\partial P_2}{\partial\epsilon}, \dots,$$

are needed to calculate the uncertainties. These are most easily found numerically, e.g.,

$$\frac{\partial u_2}{\partial\lambda} \simeq \frac{u_2(0.01,0,0,0) - u_2(0,0,0,0)}{0.01}. \tag{24}$$

Since the uncertainty in the principal Hugoniot (λ variation) originates from the data alone and the uncertainty in the off-Hugoniot corrections (ϵ variation) originates from theoretical models, they are uncorrelated. Therefore, we estimate the total systematic uncertainty by adding the two components in quadrature,

$$\sigma_{u_2\text{sys}} = \left[\left(\frac{\partial u_2}{\partial\lambda}\right)^2 + \left(\frac{\partial u_2}{\partial\epsilon}\right)^2 \right]^{1/2}, \tag{25}$$

which gives the systematic uncertainty at 1σ deviation. Similar expressions give the corresponding $\sigma_{P_2\text{sys}}$, $\sigma_{\rho_2\text{sys}}$, and $\sigma_{E_2\text{sys}}$.

Random uncertainties are determined in a similar fashion, by computing, for example,

$$\sigma_{u_2\text{ran}} = \left[\left(\frac{\partial u_2}{\partial\xi}\right)^2 + \left(\frac{\partial u_2}{\partial\zeta}\right)^2 \right]^{1/2}. \tag{26}$$

This expression and the corresponding expressions for $\sigma_{P_2\text{ran}}$, $\sigma_{\rho_2\text{ran}}$, and $\sigma_{E_2\text{ran}}$ are equivalent to the usual expressions for propagating the random errors in impedance-match expressions.[15,27]

A graphical illustration of the systematic variations is shown in Fig. 2, which shows the 1σ variations as dashed and dotted lines above and below the nominal reshock/release profile. Important to note is the inversion of the soft and stiff variations when the uncertainties are mapped onto the reshock/release profiles. For example, the stiff variation that lies above the principal Hugoniot intersects the Rayleigh
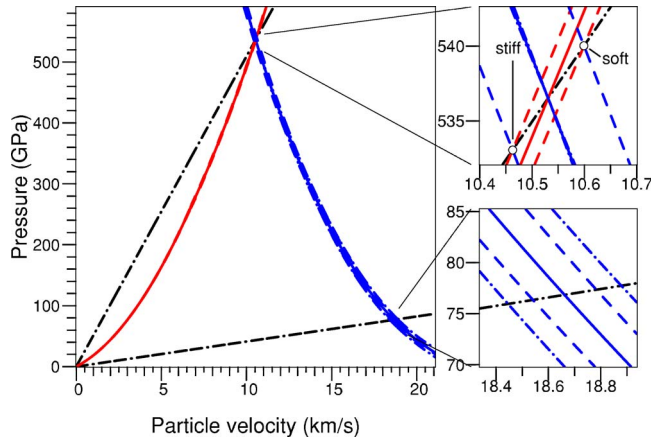
FIG. 2. (Color online) Systematics of impedance-match analysis for U_1-type measurements with a low-impedance sample. The U_1 and U_2 observables correspond to the two (dash-dot) Rayleigh lines. The principal Hugoniot (reshock-release curve) is shown as the solid red (blue) curves. Systematic variations of the principal Hugoniot are represented by the dashed curves. Systematic variations of the off-Hugoniot states are represented by the dash-dot curves. The upper right frame shows a detail of the systematics of determining the reshock-release curves from an uncertain principal Hugoniot. The lower right frame shows the impedance-match solution for a low-impedance sample.

FIG. 3. (Color online) Systematics of impedance-match analysis for u_1-type measurements with a low-impedance sample. The u_1 observable is represented by the vertical dash-dot line; other than this difference, the states are identical to those in Fig. 2, as is the meaning of the curves. In this situation the Hugoniot uncertainty is almost negligible in comparison to that in Fig. 2.

line of the incident shock with $u_1^* < u_1$ and $P_1^* < P_1$, and as a consequence it is launched below the nominal reshock/release profile. However, since it is stiffer (steeper) than the nominal profile, it tends to remain parallel. When impedance matching with very soft sample materials, the Hugoniot contribution to the systematic uncertainty can be comparable in magnitude to the uncertainty in the off-Hugoniot correction.

2. Analysis with u_1 observable

With flyer-plate experiments it is possible to accurately determine the particle velocity in the standard (largely independent of the EOS of the standard); in this case the primary observables are $u_1 \pm \delta u_1$ and $U_2 \pm \delta U_2$, i.e., the particle velocity in the standard and the shock velocity in the sample. In this case there is no systematic variation of u_1 that depends on the uncertainty of the EOS because u_1 is an observable. The parameter ξ associated with the random variation in u_1 is still required, so we define a new variable, $u_{1\xi}^* = u_1 + \xi \delta u_1$. The impedance-match equation in this case is

$$\rho_{10}[2u_{1\xi}^* - u]U^*(2u_{1\xi}^* - u; \lambda) + P_{C_1}^*(u, u_{1\xi}^*; \lambda, \epsilon) - \rho_{20}u$$

$$\times [U_2 + \zeta \delta U_2] = 0. \tag{27}$$

Solution of the equation and the determination of the partial derivatives for estimating the uncertainties are otherwise the same as expressed in Eqs. (23)–(26).

The graphical representation in Fig. 3 reveals an important difference between the two experimental cases. The shock state is identical to that in Fig. 2. However, because u_1 is fixed instead of U_1, the soft and stiff variations of the Hugoniot uncertainty produce curves on the reshock/release profile that are not inverted relative to the Hugoniot. That is, the stiff variation, which lies above the Hugoniot, also lies above the reshock/release profile and vice versa for the soft. Furthermore, because u_1 is fixed, the variation corresponding
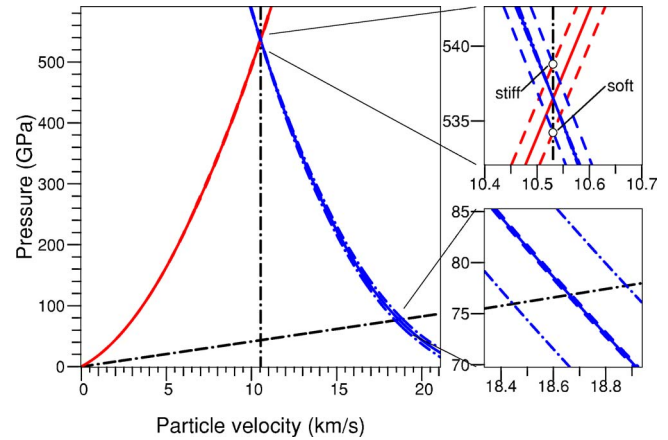
to the Hugoniot uncertainty is about $1/4 - 1/3$ that of the U_1 case. For strong release states this means that the dominant systematic uncertainty contribution is from $\sigma_{P_{C1}}(u)$, and the $\sigma_U(u)$ contribution becomes negligible.

IV. WIDE RANGE IMPEDANCE-MATCH EOS FOR ALUMINUM

Aluminum is an important impedance-match EOS standard; it is used frequently for impedance-match EOS experiments on other materials. This status has motivated a number of studies to carry out accurate absolute shock-wave EOS on Al. To construct a principal Hugoniot for the Al standard, we considered only absolute EOS measurements. A key feature of such measurements is that both the particle velocity u and shock velocity U are determined in a model-independent way. Our EOS is intended for applications primarily at pressures > 0.1 TPa, so we do not consider the data for $P < 0.03$ TPa. In the lower pressure range early experiments by Al'tshuler *et al.*[29] produced data to 200 GPa using explosively driven Fe flyer plates. Later Mitchell and Nellis[27] provided very accurate measurements from 30–170 GPa using Al and Ta flyer plates launched with a two-stage light gas gun. More recently Knudson *et al.* have produced data of nearly comparable accuracy to extend the flyer-plate data to 500 GPa (Ref. 30) and higher[31] using magnetically launched flyer plates. Above this range the experimental methods are more challenging, the available data are very sparse, and the accuracy is poorer. Simonenko and co-workers[32,33] described absolute measurements at 1 and 3 TPa; they measured the particle velocity by observing the motion of a γ source embedded in the sample as it moved past a series of collimated apertures. Podurets *et al.*[34] reported an absolute measurement of the Al Hugoniot at 1.7 TPa using an improved version of the technique described by Simonenko and co-workers. In Table I we provide a partial list the available absolute data used to generate our fits.[31] We point out that the report of Simonenko *et al.*[32] is a refined analysis of a preliminary result that appeared originally in the work Volkov *et al.*;[33]

TABLE I. Absolute shock-wave Hugoniot data for the Al shock Hugoniot for $P > 0.1$ TPa. The table lists the shock velocity U and particle velocity u with the associated measurement errors as given in the published data. This is part of the underlying data set for the fit given in Table II and is shown in Fig. 4.

U (km/s)	δU (km/s)	u (km/s)	δu (km/s)	Method	Year	Reference
7.445	0.043	1.520	0.002	Symmetric impact	1981	27
7.964	0.057	1.885	0.002	Symmetric impact	1981	27
8.810	0.056	2.522	0.003	Symmetric impact	1981	27
9.13	0.09	2.800	0.028	Symmetric impact	1960	29
9.406	0.062	2.992	0.003	Symmetric impact	1981	27
10.17	0.07	3.592	0.004	Symmetric impact	1981	27
10.39	0.10	3.700	0.037	Fe plate impact	1960	29
10.57	0.10	3.902	0.012	Ta plate impact	1981	27
11.08	0.28	4.13	0.05	Symmetric impact	2003	30
11.36	0.28	4.37	0.05	Symmetric impact	2003	30
11.25	0.11	4.382	0.013	Ta plate impact	1981	27
11.59	0.13	4.626	0.015	Ta plate impact	1981	27
11.77	0.11	4.765	0.014	Ta plate impact	1981	27
12.00	0.12	4.900	0.014	Ta plate impact	1981	27
12.04	0.13	5.007	0.016	Ta plate impact	1981	27
12.14	0.13	5.052	0.015	Ta plate impact	1981	27
12.16	0.11	5.100	0.014	Ta plate impact	1981	27
12.94	0.13	5.620	0.056	Fe plate impact	1960	29
13.77	0.45	6.38	0.07	Symmetric impact	2003	30
14.01	0.22	6.53	0.07	Symmetric impact	2003	30
14.64	0.23	7.09	0.09	Symmetric impact	2003	30
14.67	0.47	7.05	0.09	Symmetric impact	2003	30
14.91	0.24	7.21	0.09	Symmetric impact	2003	30
15.03	0.24	7.21	0.09	Symmetric impact	2003	30
15.11	0.24	7.42	0.09	Symmetric impact	2003	30
15.25	0.50	7.44	0.10	Symmetric impact	2003	30
15.23	0.50	7.50	0.10	Symmetric impact	2003	30
16.08	0.27	8.08	0.10	Symmetric impact	2003	30
17.83	0.59	9.59	0.15	Symmetric impact	2003	30
17.82	0.20	9.66	0.16	Symmetric impact	2003	30
17.89	0.20	9.81	0.18	Symmetric impact	2003	30
23.4	0.6	14.5	0.3	γ reference	1985	32
24.2	0.7	15.1	0.4	γ reference	1985	32
30.5	0.7	21.0	0.6	γ reference	1994	34
40.0	0.7	30.0	2.0	γ reference	1985	32

since the analysis of Simonenko *et al.* supersedes the result of Volkov *et al.*, we do not include the original datum of Volkov *et al.* Table I.

Besides the absolute data we note that there also exists an extensive data set of relative measurements on Al, i.e., shock measurements that are themselves impedance-match measurements relative to another standard, usually Fe, Mo, or SiO_2. We do not include these data in our fit and emphasize that only the absolute data in Table I and in Ref. 31 were used to determine the principal Hugoniot fit.

A. Principal Hugoniot of Al

It is well-known that the Hugoniot curves for many metals that do not pass through phase transitions under shock are well fitted with a piecewise linear form.[4,25] We have fitted the Al EOS data using several functional forms and used an F test to determine the optimum fit with the least number of parameters. A sequence of fitting forms with increasing numbers of parameters were tested. These were linear (two coef-

ficients), quadratic (three coefficients), piecewise linear/ linear (four coefficients), piecewise linear/quadratic (five coefficients), and piecewise quadratic/quadratic (six coefficients). The piecewise fits were determined iteratively by separating the data into upper and lower sections: points $u_i > u_{brk}$ were assigned to the upper segment and $u_i \leq u_{brk}$ to the lower segment, where u_{brk} is the particle velocity at intersection of the piecewise segments. The value of u_{brk} was determined at each iteration and then used to redivide the data for the next iteration; the iterations were terminated when u_{brk} reach a stable value (near 7 ± 1 km/s for Al). The F-test criterion (evaluated at a 10% probability cutoff) indicated that the fit was improved up to the piecewise linear/ linear case; beyond that level (e.g., linear/quadratic or quadratic/quadratic) both the data and theoretical considerations[25] do not justify the use of a higher-order fit.

The coefficients and uncertainties of the piecewise linear/linear best fit are given in Table II. The fit is also displayed in Fig. 4(a) where the solid curve shows the Al

TABLE II. Piecewise linear-linear fit to absolute measurements of the principal Hugoniot at Al. The fit was determined using procedures outlined in Secs. III A and IV and the Appendix. For the segmented linear-linear fit expressed here, the quadratic coefficients are $a_2=0$ and $\sigma_{a_2}=0$.

Fitting range (km/s)	$a_0 \pm \sigma_{a_0}$ (km/s)	$a_1 \pm \sigma_{a_1}$	β (km/s)
$u \leqslant 6.763$	9.449 ± 0.020	1.324 ± 0.016	3.0220
$6.763 < u \leqslant 30$	17.992 ± 0.078	1.167 ± 0.026	9.8381

Hugoniot fit $U(u)$, and the dashed (dotted) curves show $U(u) \pm \sigma_U(u)$ $[U(u) \pm 2\sigma_U(u)]$ together with the data points (u_i, U_i) used to generate the fit. At low pressures the data are very accurate, and the uncertainties of the fit are hidden within the width of the drawn lines. A clearer picture of the details of the fit relative to the data set is shown in Fig. 4(b), which displays the residuals $[U_i - U(u_i)]/U(u_i)$. Almost all of the data lies within 1% of the fit; a large fraction lies within 0.5%. The dashed (dotted) curves show $\pm\sigma_U(u)/U(u)$ $[\pm 2\sigma_U(u)/U(u)]$. From these curves one can see that $\pm\sigma_U(u)/U(u) < 0.5\%$ for $u < 10$ km/s, and $0.7\% < \sigma_U(u)/U(u) < 1.3\%$ for $10 < u < 32$ km/s. Because of the piecewise segmentation of the fit, the uncertainty $\sigma_U(u)$ is discontinuous at the break point ($u=6.8$ km/s); this will produce a slight discontinuity in error estimates for the data analyzed at incident shock states in Al near this discontinuity (260 GPa).

It is interesting to compare our best fit with the Hugoniot predictions from several theoretical models and fits previously published in the literature. In particular, we examine the SESAME (Ref. 26) 3719 and 3700 (Refs. 35 and 36) tabular EOS models because these have been used previously in impedance-match analysis. The 3719 table has been used by us to analyze impedance-match data previously.[8,14] The 3700 table, calculated by Kerley,[35] was used by Knudson and co-workers[15,21] to analyze impedance-match data on liquid D_2. Also shown are three other Hugoniot curves: First, a theoretical Hugoniot that appeared in the work of Mitchell *et al.*[11] was used to analyze nuclear-explosive-driven impedance-match data; this Hugoniot was extracted from Fig. 4 of that work. Second, a linear fit reported by Trunin *et al.*[37] to fit the ultrahigh pressure range given by $U = 5.9 + 1.19u$ is valid in the range $11 < u < 70$ (units in km/s). Third, a more recent wide range fit due to Trunin *et al.*[38] is used to define an Al standard for the analysis of a large set of impedance-match data, a piecewise fit given by $U = 5.333 + 1.356u$ for $u \leqslant 6.1$ and $U = 6.541 + 1.158u$ for $6.1 \leqslant u \leqslant 22$ (units in km/s). Figure 4(c) compares these models and fits by showing the relative deviation $[U_m(u) - U(u)]/U(u)$ for each model m.

At low pressures, for $u < 7$ km/s, 3719 model is clearly too soft but converges towards 3700 for $u > 10$ km/s. Both of these lie near the $U(u) + 2\sigma_U(u)$ curve for $u > 14$ km/s, which is significantly stiffer than our fit. The other SESAME tables 3713 and 3715 as well as the quotidian equation of state (QEOS) of More *et al.*[39] (not shown) also show a similar relatively stiff trend. If we focus on the range $6 < u < 22$ km/s (excluding the $u = 30$ km/s datum of Simonenko *et al.*), it is evident that our best fit, 3700, 3719, and
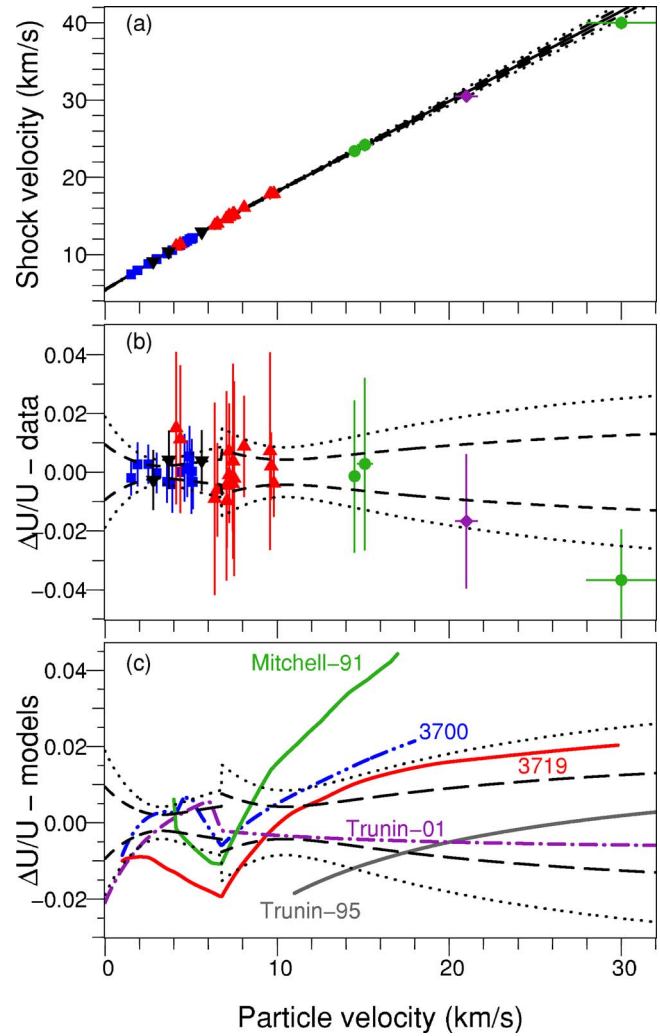

FIG. 4. (Color online) (a) Absolute Al Hugoniot data in the U-u plane, from Ref. 29—inverted triangles, Ref. 27—solid squares, Ref. 30—solid triangles, Ref. 32—solid circles, and Ref. 34—solid diamond. The piecewise linear best fit is the solid black line; the $\pm\sigma_U$ ($\pm 2\sigma_U$) uncertainty limits are delimited by the black dashed (dotted) curves. (b) Residuals $[U_i - U(u_i)]/U(u_i)$ of the Hugoniot data and the relative uncertainties of the fit: $\pm\sigma_U/U$ (dashed) and $\pm 2\sigma_U/U$ (dotted). (c) Similar to (b) showing the relative deviations of several Al EOS models from the best fit: $[U_m(u) - U(u)]/U(u)$. References to the labeled curves are Mitchell-91 (Ref. 11) (solid, green), 3700 (Ref. 35) (dash-dot-dot, blue), 3719 (Ref. 26) (solid, red), Trunin-95 (Ref. 37) (dash-dot, magenta), and Trunin-01 (Ref. 38) (solid, grey).

Trunin-01 pass through the error bars of almost all the points in this range; thus it can be claimed that all of the models (excluding Mitchell-91) are in good agreement with the data. The reduced χ_ν^2 statistics evaluated for each of these models relative to the data in the range $6 < u < 22$ km/s have values of $\chi_{\nu_F}^2 = 0.138$ for our best fit and $\chi_{\nu_m}^2 = 0.177$, 0.361, and 0.405 for Trunin-01, 3700, and 3719, respectively (here $\nu = 23$, given 25 data points, and assuming a linear two-parameter form represents the model in the range). Since $\chi_\nu^2 < 1$ for all cases, all the models represent good fits. However, the fact that χ_ν^2 is significantly less than unity in all cases indicates that the given error bars are overestimated; therefore, the χ_ν^2 statistics are not useful for distinguishing between models. A more meaningful question is what is the probability that model A is more correct than model B rela-

TABLE III. Coefficients for the pressure correction in shock compressed Al as expressed in Eqs. (17) and (18). For each impedance-match experiment the coefficients for the pressure correction and its uncertainty are determined by linear interpolation in this table, using the particle velocity u_1 in the shock incident in the standard as the independent variable.

u_1 (km/s)	b_{s1} $(\sigma_{b_{s1}})$ $(\times 10^{-3})$	b_{s2} $(\sigma_{b_{s2}})$ $(\times 10^{-3})$	b_{r1} $(\sigma_{b_{r1}})$ $(\times 10^{-3})$	b_{r2} $(\sigma_{b_{r2}})$ $(\times 10^{-3})$	b_{r3} $(\sigma_{b_{r3}})$ $(\times 10^{-3})$
0	0 (00)	0.0 (0.0)	0.0 (0.0)	0.0 (0.0)	0.0 (0.0)
2	−1 (00)	0.0 (0.3)	4.5 (3.8)	−0.8 (2.7)	−1.3 (2.1)
4	−23 (11)	3.3 (1.0)	20.1 (11.9)	−3.8 (3.9)	−2.3 (1.5)
6	−75 (06)	15.4 (4.0)	22.4 (7.5)	−0.8 (5.8)	−4.3 (1.3)
8	−112 (19)	22.2 (4.7)	27.8 (9.0)	1.6 (6.7)	−7.5 (2.8)
10	−142 (25)	28.1 (2.0)	29.2 (6.2)	4.7 (6.3)	−7.6 (3.1)
12	−171 (22)	36.0 (3.9)	30.4 (6.2)	5.2 (6.3)	−9.0 (2.9)
14	−201 (20)	43.3 (4.3)	31.6 (6.2)	5.7 (6.1)	−9.9 (2.6)
16	−228 (20)	48.6 (4.2)	32.4 (6.3)	5.8 (6.0)	−10.5 (2.2)
18	−253 (22)	52.9 (3.7)	33.2 (6.2)	5.9 (6.0)	−11.2 (1.7)
20	−277 (25)	57.2 (5.3)	33.7 (6.0)	6.2 (6.2)	−11.8 (1.2)
22	−311 (17)	61.9 (7.2)	33.4 (6.0)	6.1 (7.5)	−12.6 (0.7)
24	−333 (24)	64.4 (9.7)	34.2 (5.0)	5.8 (9.1)	−12.7 (0.6)
26	−350 (28)	66.9 (11.8)	35.1 (4.2)	7.6 (7.7)	−14.3 (0.8)
28	−367 (27)	71.2 (10.0)	35.7 (2.6)	8.7 (8.6)	−15.5 (1.4)
30	−386 (25)	76.9 (5.1)	35.6 (1.8)	10.3 (7.5)	−16.2 (1.9)
32	−407 (25)	82.4 (1.5)	36.0 (1.5)	10.5 (5.8)	−16.4 (2.6)

tive to the given data set? This question can be answered by performing an F test, that is, by computing $P_F(F, \nu_1, \nu_2)$ where P_F is the F-distribution probability for exceeding F and $F = \chi^2_{\nu_m}/\chi^2_{\nu_F}$ is the ratio of the two χ^2_ν statistics with ν_1 and ν_2 are degrees of freedom, respectively.[40] In our case $\nu_F = \nu_m = 23$. We find probabilities of 28%, 1.3%, and 0.6% that the Trunin-01, 3700, and 3719 models, respectively, are better representations of the data than our best fit in the range $6 < u < 22$ km/s. In other words, this suggests >98% probability that 3700 and 3719 are too stiff relative to the existing data set.

B. Pressure corrections

The pressure corrections for our Al EOS were generated by averaging the pressure corrections predicted by five different EOS models using the method described in the Appendix. The results are tabulated as a set of fitting coefficients, listed in Table III, and are used in Eqs. (16)–(19) to produce quantitative evaluations of the pressure correction $P_{C_1}(u)$. The pressure corrections were averaged over a set that included SESAME models 3713, 3715, and 3719; Kerley's 3700 table;[35,36,41] and the QEOS model.[39] Figure 5 shows the systematic trends of the pressure corrections. At low shock amplitudes ($u_1 \leq 4$ km/s) the magnitude of the pressure correction is less than 3% for all values of q, indicating that the mirror-reflection approximation is accurate at low pressures. At higher pressures the correction increases significantly on the reshock branch, especially for large impedance mismatches: for $q < -0.5$ it exceeds 40% of P_1 for $u_1 > 25$ km/s. On the release branch, however, the magnitude of the correction never exceeds 5% of P_1 for all values of q; however, one should be aware that $P_2 \ll P_1$ for large q, so the correction is significant relative to P_2. Also notable is the fact

that $p_{n_1}(q) > 0$ for all q at low shock amplitudes, while at higher amplitudes the correction curve takes on a characteristic oscillation: There is a finite range $0 \leq q \leq 0.5$ where $p_{n_1}(q) < 0$ on the release branch. The pressure correction is entirely model dependent; therefore, it is important to compare the correction against available data in order to assess its validity.

1. Reshock branch

In Figs. 6(a)–6(c) plotted is a series of reshock data measured by Nellis *et al.*[42] for double-shocked Al using Ta and Cu anvils. The experiments determined the reshock state $(u_2 \pm \delta u_2, P_2 \pm \delta P_2)$ produced from a known incident shock state (u_1, P_1) by observing the shock state in an anvil whose EOS has previously been determined. By constructing the quantity $[P_2 - P_{M_1}(u_2)]/P_H(u_1)$ we obtain an experimental determination of the pressure correction relative to the mirror reflection of our best-fit Hugoniot; in the figure this is plotted versus the normalized particle velocity $q_2 = u_2/u_1 - 1$, where P_{M_1} and P_H are defined in Eqs. (7), (6), and (14) and Table II. Since u and q are regarded as independent variables, the measurement error δu_2 is incorporated into the uncertainty in the measured pressure correction,

$$\delta_{p_{n_1}}(q_2) = \frac{1}{P_H(u_1)} \sqrt{(\delta P_2)^2 + (dP_{R_1}/du|_2)^2 (\delta u_2)^2}, \quad (28)$$

where $dP_{R_1}/du|_2$ is the slope of the Al reshock curve at the $u = u_2$ measurement state. The datum in Fig. 6(d) compares a reshock point at 1.4 TPa reported by Trunin *et al.*[37] No uncertainties were reported for the latter point; these were estimated by assuming the same relative errors as reported by Nellis *et al.* For the range of velocities and pressures for which the data are available, the pressure corrections are in
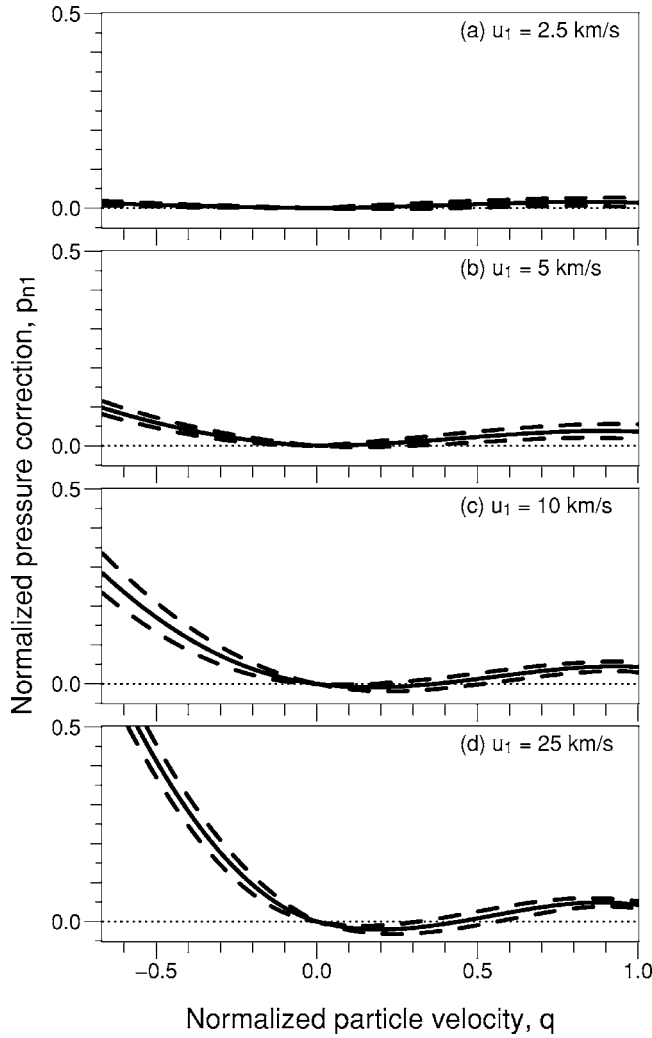
FIG. 5. Solid curves show normalized pressure correction $p_{n_1}(q)$ for reshock and release profiles centered on states with (a) $u_1=2.5$ km/s, (b) $u_1=5$ km/s, (c) $u_1=10$ km/s, and (d) $u_1=25$ km/s. Upper (lower) dashed curves show the curves $p_{n_1}(q)+(-)\sigma_{p_{n_1}}(q)$, delimiting the $\pm 1\sigma$ uncertainty band of the pressure correction.

agreement within the accuracy of the data; however, it is evident the data are sparse and the accuracy is not high enough to distinguish between models or to assess the overall accuracy of the reshock pressure correction. Nellis *et al.* concluded that the data are in very good agreement with the mirror-reflection approximation. Given that there is no significant discrepancy and that the deviation among the models is smaller than the data accuracy, we can only assume that the models provide a good representation of the reshock states.

2. Release branch

For the release branch the most stringent test of the pressure correction is for strong releases. Figure 7 shows a comparison of the release branch pressure correction against the data of Holmes[43] and Knudson *et al.*,[21] who measured the release state $(u_2\pm\delta u_2, P_2\pm\delta P_2)$ of Al releasing into a SiO$_2$ aerogel foam sample with a known EOS. The measurement uncertainties δp_{n_1} were calculated as in Sec. IV B 1 with Eq.

(28). The measurements were from initial states at $u_1=3$ km/s and $u_1=6.44$, 7.5, and 10 km/s, respectively. It is instructive to focus on Fig. 7(d) where there are a statistically useful number of data points clustered around $q=0.76$. Here we find that the statistical average of the seven data points (0.036) matches very closely the average theoretical correction (0.037), and that the standard deviation of the seven data points (0.015) matches closely the standard deviation among the theories (0.013). Therefore, the model-averaged release correction is accurate, and the available data provide no justification to modify the theoretical content (e.g., to impose a bias by eliminating or favoring particular models). The fact that the standard deviations are comparable is fortuitous but also convenient; since the error bars and standard deviation of the data are well matched to the standard deviation among the theoretical models, we can use $\sigma_{pc_1}(u)$ from the models without modification as close representation of the true (i.e., experimental *and* theoretical) uncertainty in the pressure corrections of the release branch. This also indicates that the current measurement accuracies, as impressive as they are, remain insufficient to distinguish among the five theoretical models examined in this study.

C. Thermodynamic derivatives

The empirical EOS construction developed here is intended primarily for data analysis and to produce accurate error estimates; it avoids explicit model-dependent functional forms (e.g., Mie-Grüneisen) with the aim of producing neutrally biased fits. Nevertheless, it is useful to make contact with current theoretical models of the high-pressure Al EOS. Since the current model provides a description of states both on and off the principal Hugoniot, it is possible to extract thermodynamic derivatives, specifically the isentropic sound velocity c_s, the Grüneisen coefficient Γ, and the $\hat{U}$ vs Δu relationships of the second shock Hugoniot curves.

Thermodynamic derivatives can be expressed as algebraic combinations of various derivatives taken with respect to u along the principal Hugoniot and along the reshock/release curves, i.e., the derivatives dP_H/du, dP_{R_1}/du, etc. It is useful at this point to introduce expressions giving the volume and energy along the principal Hugoniot. These are

$$V_H(u) = \frac{U(u)-u}{\rho_{10}U(u)}, \tag{29}$$

$$E_H(u) = E_{10} + \frac{1}{2}[P_H(u)+P_{10}]\left[\frac{1}{\rho_{10}} - V_H(u)\right], \tag{30}$$

where $U(u)$ is the Hugoniot fit of Eq. (14) and $P_H(u)$ is from Eq. (6). The corresponding expressions along the reshock Hugoniot are

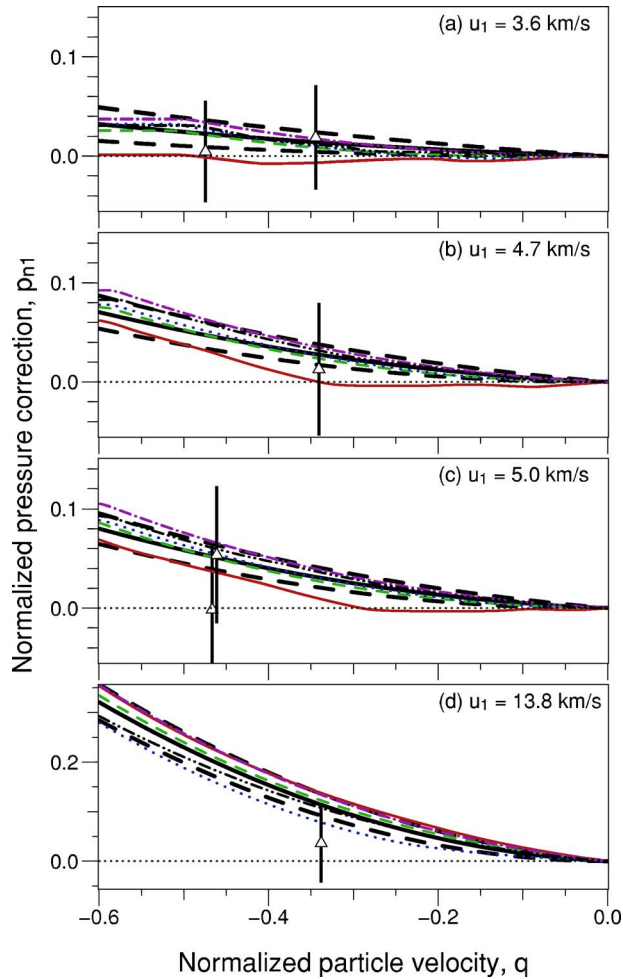$$V_{R1}(u) = V_H(u_1) - (u-u_1)^2/[P_{R_1}(u)-P_H(u_1)], \tag{31}$$

FIG. 6. (Color online) Al double shock data (open triangles) in (a)–(c) are from Ref. 42 and in (d) from Ref. 37. The light curves show pressure corrections predicted from individual theoretical models: 3715 (solid, red), 3719 (dash, green), 3713 (dot, blue), QEOS (dash-dot, magenta), and 3700 (dash-dot-dot, black). The heavy solid curves show $p_{n_1}(q)$ and the heavy dashed curves show $p_{n_1}(q) \pm \sigma_{p_{n1}(q)}$.
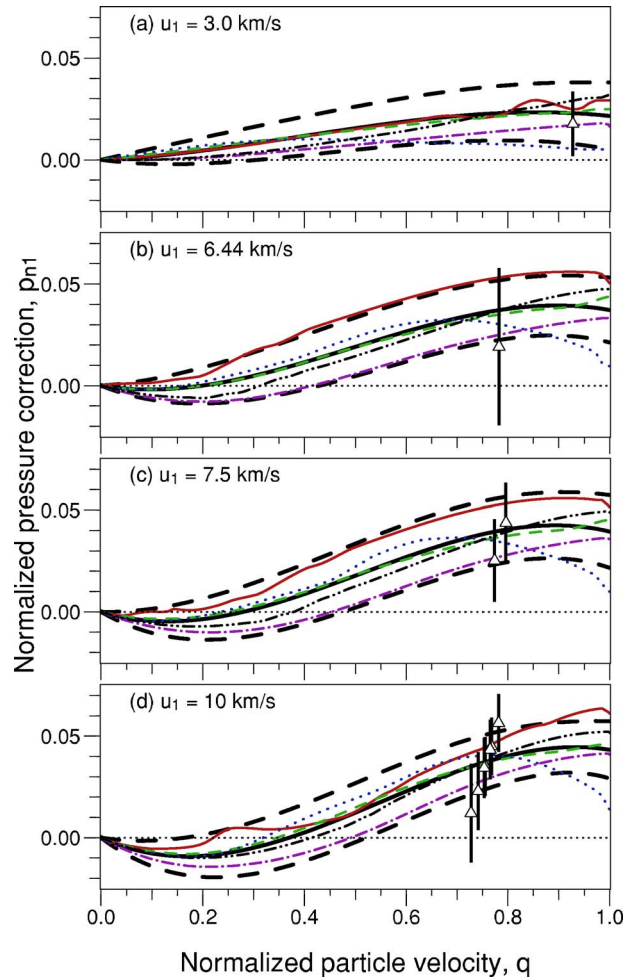

FIG. 7. (Color online) Al release profile data (open triangles) in (a) is from Ref. 43 and in (b)–(d) from Refs. 15 and 21. The curves are as indicated in the caption for Fig. 6.

$$E_{R1}(u) = E_H(u_1) + \frac{1}{2}[P_H(u_1) + P_{R_1}(u)]$$

$$\times [V_H(u_1) - V_{R1}(u)], \tag{32}$$

where $P_{R_1}(u)$ is as given by Eqs. (8), (16), and (17). We develop the thermodynamic derivatives using the reshock branch rather than the release branch because simple analytic expressions are easily derived for the thermodynamic quantities using the Rankine-Hugoniot equations. It is not possible to derive such simple expressions on the release branch, because integrations along isentropes are required. However, in the limit of weak shocks, the second shock Hugoniot follows the isentrope very closely.

In the process of evaluating the derivatives of these terms, it is also convenient to express the pressure correction in the form of a Taylor series expanded about $q = u/u_1 - 1$,

i.e., about states (u_1, P_1) along the principal Hugoniot. To second order in q the pressure correction can be expressed as

$$p_{n_1}(q) = Aq + Bq^2, \tag{33}$$

where the coefficients A and B and their respective uncertainties are expressed in terms of the reshock pressure correction coefficients,

$$A = 3b_{s1} + 12b_{s2}, \quad \sigma_A = [9\sigma_{b_{s1}}^2 + 144\sigma_{b_{s2}}^2]^{1/2},$$

$$B = 18b_{s2}, \quad \sigma_B = 18\sigma_{b_{s2}}. \tag{34}$$

Here it is implicit that A and B are functions of u_1 (since b_{si} and b_{ri} are functions of u_1). Over the range of particle velocities listed in Table III A varies from 0 to -0.22, and σ_A varies from 0 to 0.17.

In the expressions below we give expressions valid only for a linear segment of the u-U shock Hugoniot. The sound speed is connected with the acoustic impedance and the compressibility, which in turn is related to the slope dP_{R_1}/du of the reshock/release curve,

$$c_s(u_1) = V_H(u_1) \left. \frac{dP_{R1}}{du} \right|_{u=u_1} = \frac{[a_0 + (a_1 - 1)u_1 - a_1\beta]\{(A-1)a_0 + a_1[(A-2)u_1 + (1-A)\beta]\}}{a_0 + a_1(u_1 - \beta)}. \tag{35}$$

The Grüneisen coefficient Γ is defined as $\Gamma = V \partial P/\partial E|_V$; this quantity can be derived in a similar fashion from the principal Hugoniot and reshock/release curves,

$$\Gamma(u_1) = V_H(u_1) \frac{(dP_H/du)(dV_H/du)^{-1} - (dP_{R_1}/du)(dV_{R_1}/du)^{-1}}{(dE_H/du)(dV_H/du)^{-1} - (dE_{R_1}/du)(dV_{R_1}/du)^{-1}} \Bigg|_{u=u_1}$$

$$= \frac{1}{a_1 u_1^2 [a_0 + a_1(u_1 - \beta)]^2} \Bigg[[a_0 + (a_1 - 1)u_1 - \beta a_1](a_1\beta - a_0)$$

$$\times \left(-\frac{[a_0 + a_1(u_1 - \beta)]^2 [a_0 + a_1(2u_1 - \beta)]}{a_0 - a_1\beta} + \{(A-1)a_0 + a_1[(A-2)u_1 - (A-1)\beta]\}^2 \right) \Bigg]. \tag{36}$$

Both c_s and Γ are first derivatives of the pressure on the EOS surface, and as such they depend only on the first derivatives of P_{R_1}, P_H, E_{R_1}, E_H, etc., evaluated along the Hugoniot (i.e., $u \to u_1$). Therefore, the expressions for c_s and Γ have no dependence on B, the second-order term of Eq. (33). Furthermore, most of the dependence involves the parameters of the principal Hugoniot fit (a_0, a_1 and β), with a small sensitivity to the precise value of A. Thus the model-dependent contributions to the expressions for c_s and Γ are small; the derived values depend primarily on the fit to the principal Hugoniot and therefore on the absolute shock Hugoniot data. The uncertainties of c_s and Γ are easily calculated from the uncertainties in the underlying parameters, e.g., $\delta c_s = [\sigma_A^2(\partial c_s/\partial A)^2 + \Sigma_i \sigma_{a_i}^2(\partial c_s/\partial a_i)^2]^{1/2}$.

Figure 8 shows c_s and Γ along the principal Hugoniot to 3 TPa. The experimental sound speed data of McQueen *et al.*[44] are in excellent agreement; the Grüneisen parameter measurements of Neal[45] are also in good agreement except near the melt transition. Notable in Fig. 8(a) is that above 0.5 TPa c_s is somewhat smaller than the average value predicted by the theoretical models. This is expected because the piecewise fit to the Hugoniot is significantly softer than the Hugoniot curves predicted by the models. The uncertainty in c_s is quite large at high shock pressures and reflects the fact that the fit is less accurate at higher pressures. The dashed curve, lying below the c_s curve, is the result if we set $A=0$ in Eq. (35); this is equivalent to assuming that the mirror-reflection approximation holds true along the Hugoniot. The fact that this latter curve lies close to the c_s points indicates that the model-dependent pressure corrections play a minor role in determining c_s, and that the fit to the Hugoniot data determines most of the compressibility.

Shock Hugoniot curves for second shocks closely follow a linear $\hat{U}$ vs Δu dependence, $\hat{U}(|\Delta u|) = c_s + \hat{s}|\Delta u|$, where $\hat{U}$ is the velocity of the second shock relative to the medium behind the first shock and $\Delta u = u - u_1$ is the change in particle speed between the first shock and second shock states. The slope $\hat{s}(u_1)$ is given by the equation

$$\hat{s}(u_1) = \frac{d}{du} \left[V_H(u_1) \frac{P_{R_1}(u) - P_H(u)}{u - u_1} \right] \Bigg|_{u=u_1}$$

$$= \frac{\{a_1 u_1 + B[a_0 + a_1(u_1 - \beta)]\}[a_0 + (a_1 - 1)u_1 - a_1\beta]}{u_1[a_0 + a_1(u_1 - \beta)]}. \tag{37}$$

Evident from this expression is that $\hat{s}$ depends on the second-order coefficient B and has no dependence on A. Figure 9 shows a plot of the second shock Hugoniot slope. Above $P \sim 0.5$ TPa, the correction introduces a large adjustment to the estimated value of $\hat{s}$, indicating a large model-dependent contribution. In general second shock states for reshock-type impedance-match experiments are not "strong" relative to the first shock state, because $P_2 \sim P_1$. Since B is a second-order correction, it is related to a second derivative of the EOS surface. A Taylor expansion in u of the Hugoniot carried out by Johnson[25] (weak shock limit) relates $\hat{s}$ to the isentropic pressure derivative of the bulk modulus, $\partial B_S/\partial P|_s = 4\hat{s} - 1$, where B_S is defined as $B_S = \rho \partial P/\partial \rho|_s$. Evidently, for shocked Al near 3 TPa, $\partial B_S/\partial P|_S \simeq 2.6$.

V. EXAMPLES

The best-fit Hugoniot is softer than the available tabular models for Al at pressures above 1 TPa. Therefore, application of this model to existing data reaching into the terapascal range is of interest, because all previous analyses have used tabular EOS models that are probably too stiff. More importantly, the examples serve to provide quantitative estimates of the systematic uncertainties in addition to the random uncertainties. We show the relative contributions of these error sources for several relevant cases.

A. Example: High-pressure EOS of Cu and Mo

High-pressure nuclear impedance-match data for Cu and Mo relative to Al were measured by Mitchell *et al.*[11] and analyzed with a theoretical EOS for Al that was constructed by the authors of that work. The principal Hugoniot in Ref. 11 is significantly stiffer than our current best-fit model, corresponding to $\sim U(u) + 5\sigma_U(u)$ [see Fig. 4(c)].
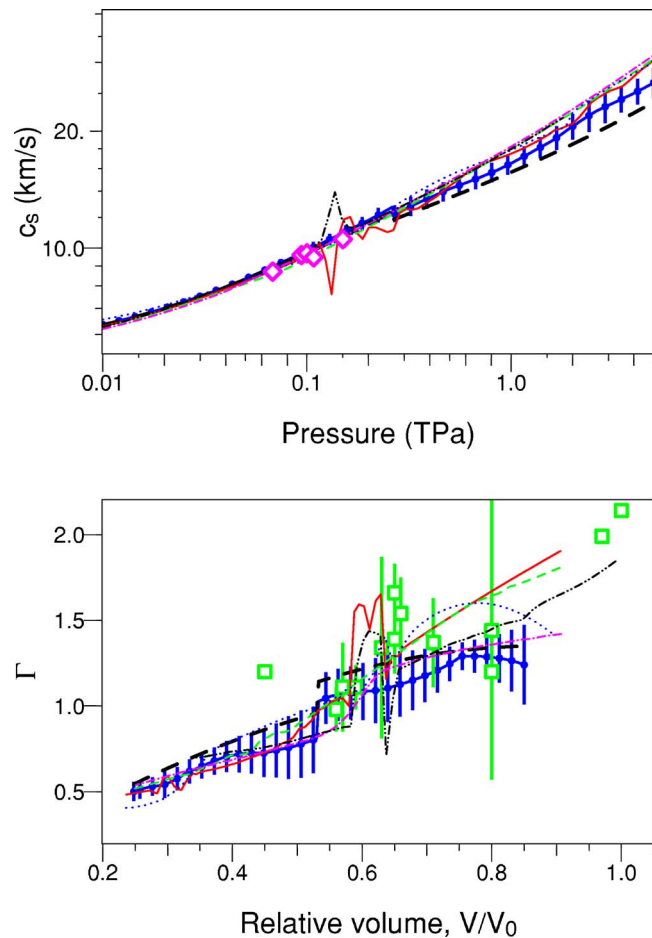
FIG. 8. (Color online) (a) Solid circles show the sound velocity c_s predicted by Eq. (35); the uncertainty in c_s is indicated by the error bars. The light curves show c_s as predicted from individual theoretical models: 3715 (solid, red), 3719 (dash, green), 3713 (dot, blue), QEOS (dash-dot, magenta), and 3700 (dash-dot-dot, black). Both 3715 and 3700 contain a realistic description of the melt transition; this produces the oscillations near 0.15 TPa. The heavy dashed curve shows c_s from (35) for the case when $A=0$. The open diamonds show the bulk sound speed data of McQueen *et al.* (Ref. 44). (b) Solid circles show the Grüneisen coefficient Γ predicted by Eq. (36). Open squares with error bars show the data reported by Neal (Ref. 45). The remaining curves have the same correspondence to the models as in (a).
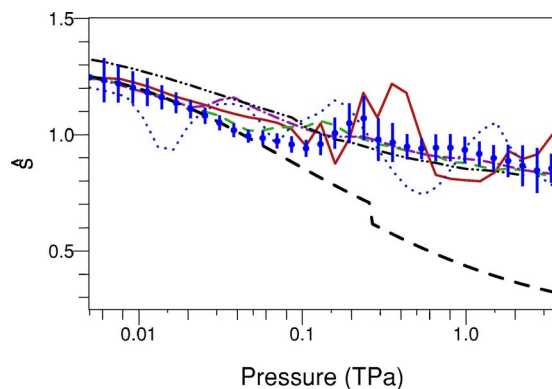

FIG. 9. (Color online) Filled circles show the slope $\hat{s}$ of the second shock Hugoniot given by Eq. (37), plotted as a function of shock pressure. Error bars indicate the uncertainty in $\hat{s}$. Light curves are from models as in Fig. 8. Heavy dashed curve shows the value of $\hat{s}$ expected for the mirror-reflection approximation, $B=0$.
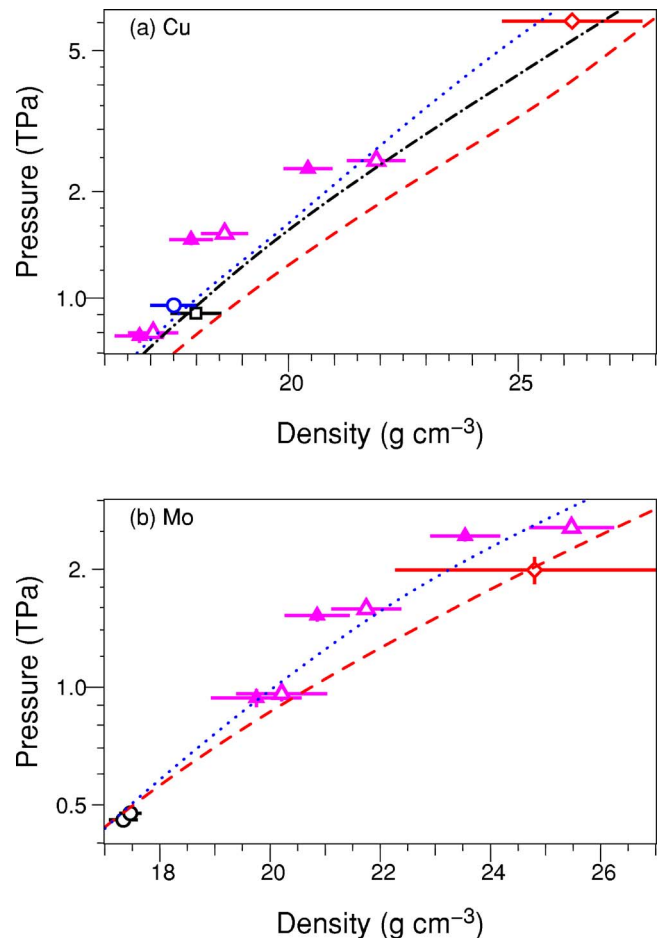

FIG. 10. (Color online) (a) Hugoniot data for Cu on the P-ρ plane. The original analysis by Mitchell *et al.* (Ref. 11) is given by the solid triangles; the reanalyzed data are shown by the open triangles. The error bars represent only the random error contribution. Curves show the Hugoniots from three different SESAME EOS models: 3330 (dashed, red); 3332 (dotted, blue); and 3333 (dash-dot, black). The data points are open diamond (Ref. 10), open square (Ref. 49), and open circle (Ref. 50). (b) Hugoniot data for Mo, triangles, as in (a). Curves are from SESAME models for Mo: 2980 (dashed, red) and 2981 (dotted, blue). Data points: open diamond (Ref. 51); open circles are the (absolute) gas gun data reported in Ref. 11.

The raw measurement data was published in Table II of Ref. 11, and thus it is possible to reanalyze these data using our impedance-match model. The results of this reanalysis are shown in Fig. 10(a) for the Cu case and Fig. 10(b) for the Mo case. In addition the detailed results of the impedance-match analysis are given in Table IV. For both the Cu and Mo experiments the reanalysis produces a general softening of the Cu and Mo Hugoniot points, with the largest shift occurring at the highest pressures; analysis of these points (at ~2.5 TPa) produces approximately 8% higher compression than the original analysis. The original data as published in Refs. 11 were significantly stiffer than other experiments and existing tabular models, a fact that has been noted by others;[46] the analysis brings these impedance-match data into closer agreement with the existing data and models.

A comparison of the relative contributions of the four sources of error is of interest to experimentalists designing future experiments. The contributions from the two systematic error sources are balanced and produce a total systematic uncertainty of about 1.5% in the determination of compres-

TABLE IV. Analysis of the impedance-match data from Table II of Mitchell *et al.* (Ref. 11). Raw data are displayed in columns two to five; the analysis results are in the adjoining columns. Columns six to nine show a breakdown of the individual error contributions in the determination of σ_{u_2} including the contributions from the measurement errors of the two observables, $\partial u_2/\partial \xi$ and $\partial u_2/\partial \zeta$, the systematic uncertainty contribution of the Hugoniot fit $\partial u_2/\partial \lambda$, and the systematic uncertainty contribution of the off-Hugoniot (reshock) curve $\partial u_2/\partial \epsilon$. Uncertainties in the last one or two digits are enclosed in parentheses. Random and systematic uncertainties, denoted by (ran, sys), for u_2 are given by Eqs. (26) and (25), respectively. A similar decomposition of contributions can be computed for other variables. P_2, ρ_2, E_2, etc., and is given for P_2 and the compression $\eta_2 = \rho_2/\rho_{20}$.

Expt.	ρ_{10}	ρ_{20}	$U_1(\delta U_1)$	$U_2(\delta U_2)$	$\dfrac{\partial u_2}{\partial \xi}$	$\dfrac{\partial u_2}{\partial \zeta}$	$\dfrac{\partial u_2}{\partial \lambda}$	$\dfrac{\partial u_2}{\partial \epsilon}$	u_2 (ran, sys)	P_2 (ran, sys)	η_2 (ran, sys)
	(g cm^{-3})		(km/s)		(km/s $\times 10^{-3}$)				(km/s)	(GPa)	
Cu-1	2.714	8.938	28.00(20)	21.50(20)	167	−54	−131	75	12.74(18,15)	2448(34,29)	2.45(7,4)
Cu-2	2.697	8.934	22.90(20)	18.10(20)	161	−50	−69	55	9.42(17,09)	1523(27,14)	2.08(5,2)
Cu-3	2.699	8.937	17.90(20)	13.70(20)	158	−48	−44	49	6.53(17,07)	799(20,08)	1.91(6,2)
Mo-1	2.714	10.150	28.00(20)	20.50(20)	162	−57	−126	76	12.27(17,15)	2554(36,31)	2.49(7,4)
Mo-2	2.697	10.220	22.90(20)	17.10(20)	157	−53	−66	56	9.06(17,09)	1584(29,15)	2.13(6,2)
Mo-3	2.699	10.220	18.90(30)	13.80(20)	230	−51	−41	53	6.82(24,07)	962(33,09)	1.98(8,2)

sion. The measurement error is larger; furthermore, the magnitude of $\partial u_2/\partial \xi$ is about three times larger than $\partial u_2/\partial \zeta$, indicating that most of the random error contribution comes from propagating the uncertainty δU_1. This is because the Rayleigh line for the incident shock intersects the Al principal Hugoniot at an acute angle, which tends to magnify the contribution of δU_1. Since the Rayleigh line of the shock in the sample tends to intersect the reshock-release curves at much larger angles, the propagated contribution of δU_2 is much smaller. This is true in general for all U_1-type measurements. Therefore, optimized impedance matching with U_1-type measurements will be obtained with experiments optimized, if possible, to maintain $\delta U_1 \simeq 0.2-0.3\,\delta U_2$.

Reduction of the measurement uncertainty to a level much below that of the systematic uncertainty (for this particular case) is probably not warranted. Although one might expect future improvement in our knowledge of the principal Hugoniot of Al, the uncertainty in the off-Hugoniot correction, as noted in Sec. IV B, is not likely to change without a significant improvement in measurement accuracies. This assessment must be made on a case to case basis for different samples and drive pressures.

B. Example: High-pressure EOS of LiF and Al$_2$O$_3$

Laser-driven shock-wave experiments on LiF (to 1.4 TPa) and Al$_2$O$_3$ (to 1.9 TPa) were carried out recently using an Al reference standard.[14] These experiments were analyzed using the SESAME 3719 table. The raw observational data (U_1 and U_2) from these experiments was indicated in Fig. 1 of Ref. 14. We have reanalyzed these data using our impedance-match model in order to infer more accurate values for the compression and to provide estimates of the systematic uncertainties.

The results, listed in Table V, produce slightly higher compressions owing to the fact that 3719 lies near $U(u) + 2\sigma_U(u)$ relative to our best fit in this pressure range. The LiF compression is about 3% higher and the Al$_2$O$_3$ compression is about 2% higher. The results also show that the systematic error in this case is dominated by the uncertainty in the principal Hugoniot ($\partial u_2/\partial \lambda$); this is especially so in the case of LiF which is well matched in impedance to the Al reference. The total systematic uncertainty in compression is about 1.5%–2%, about a factor of 4 smaller than the measurement uncertainty.

The measurement errors are dominated by the uncertainty in the measurement of U_1 because $\partial u_2/\partial \xi \sim 10 \partial u_2/\partial \zeta$; in these experiments transit-time measurements across a stepped base plate were used to determine U_1 with about 2%–2.5% accuracy. The measurement uncertainties can be improved by concentrating on improving the measurement accuracy of U_1; methods to achieve this are under active development.

TABLE V. Analysis of the impedance-match data from Fig. 1 of Hicks *et al.* (Ref. 14). The column arrangement is the same as in Table IV.

Expt.	ρ_{10}	ρ_{20}	$U_1(\delta U_1)$	$U_2(\delta U_2)$	$\dfrac{\partial u_2}{\partial \xi}$	$\dfrac{\partial u_2}{\partial \zeta}$	$\dfrac{\partial u_2}{\partial \lambda}$	$\dfrac{\partial u_2}{\partial \epsilon}$	u_2(ran,sys)	P_2(ran,sys)	η_2(ran,sys)
	(g cm^{-3})		(km/s)		(km/s $\times 10^{-3}$)				(km/s)	(GPa)	
Al$_2$O$_3$−1	2.70	3.97	29.27(84)	28.57(23)	829	−52	−191	55	17.12(83,20)	1942(95,23)	2.50(19,04)
Al$_2$O$_3$−2	2.70	3.97	26.99(39)	26.27(22)	384	−50	−156	43	15.40(39,16)	1606(41,17)	2.42(09,04)
Al$_2$O$_3$−3	2.70	3.97	22.19(45)	22.65(28)	431	−58	−84	38	11.51(43,09)	1035(39,08)	2.03(09,02)
LiF−1	2.70	2.64	27.04(69)	29.26(32)	736	−66	−178	9	17.25(74,18)	1332(58,14)	2.44(16,04)
LiF−2	2.70	2.64	27.93(72)	29.55(26)	774	−56	−195	6	18.14(78,20)	1415(61,15)	2.59(18,04)
LiF−3	2.70	2.64	25.60(47)	26.61(28)	506	−60	−156	3	16.26(51,16)	1143(36,11)	2.57(14,04)

TABLE VI. Analysis of a subset of eight experiments from the impedance-match data of Knudson *et al.* (Ref. 15). Data are from Table I in Ref. 15. The column arrangement is the same as given in Table IV. The principal Hugoniot of the Al standard was adjusted slightly for cryogenic conditions (higher density and a small correction to the slope).

Expt.	ρ_{10}	ρ_{20}	$U_1(\delta U_1)$	$U_2(\delta U_2)$	$\frac{\partial u_2}{\partial \xi}$	$\frac{\partial u_2}{\partial \zeta}$	$\frac{\partial u_2}{\partial \lambda}$	$\frac{\partial u_2}{\partial \epsilon}$	$u_2(\text{ran},\text{sys})$	$P_2(\text{ran},\text{sys})$	$\eta_2(\text{ran},\text{sys})$
	(g cm^{-3})		(km/s)		(km/s$\times 10^{-3}$)				(km/s)	(GPa)	
Z904N	2.74	0.167	5.27(13)	13.50(24)	250	−17	5	128	9.69(25,13)	21.9(0.7,0.3)	3.55(29,12)
Z590	2.74	0.167	6.38(29)	15.26(28)	553	−22	6	145	11.69(55,14)	29.8(15,0.4)	4.27(72,17)
Z792S	2.74	0.167	7.42(15)	17.91(39)	287	−33	8	186	13.46(29,19)	40.3(1.2,0.6)	4.03(39,17)
Z711	2.74	0.167	9.98(25)	23.23(19)	474	−18	7	208	17.80(47,21)	69.1(1.9,0.8)	4.28(40,16)
Z894	2.74	0.167	10.35(16)	24.10(22)	303	−21	7	215	18.42(30,21)	74.1(1.4,0.9)	4.24(27,16)
Z1111N	2.74	0.167	10.80(17)	24.94(44)	316	−43	7	224	19.18(32,22)	79.9(1.8,0.9)	4.33(37,17)
Z1110N	2.74	0.167	11.37(17)	26.11(47)	318	−46	7	235	20.14(32,24)	87.8(2.0,1.0)	4.37(38,17)
Z946	2.74	0.167	12.12(49)	28.00(57)	927	−56	8	249	21.38(93,25)	100.0(4.7,1.2)	4.23(67,16)

C. High-pressure EOS of liquid deuterium, flyer-plate method

A recent series of impedance-match experiments on liquid deuterium (D_2) were reported by Knudson *et al.*[15] In those experiments the shock was driven by a magnetically accelerated flyer plate, which impacted an Al base plate from which the shock was transmitted in the D_2 sample. Measurements of the flyer-plate velocity were used to determine $u_1 \pm \delta u_1$ and measurements of the shock velocity in the D_2 determined $U_2 \pm \delta U_2$. From these inputs an impedance-match analysis following the procedure outlined in Sec. III C 2 can be carried out. The experiments of Knudson *et al.* were analyzed using Kerley's 3700 table for the Al EOS.

A quantitative assessment of the systematic uncertainties was not carried out in Ref. 15, primarily because of the difficulties summarized in the Sec. II B. Therefore, we have reanalyzed a subset of the data presented in Ref. 15 to compare with our impedance-match model and to estimate the magnitude of the systematic error present in the analysis of that experiment. Knudson *et al.* estimated the systematic uncertainty in the compression to be a few percents and backed up this assessment with reverberation measurements that corroborated their density determination. Reanalysis of their data for a subset of eight experiments is given in Table VI. Examination of this table in comparison with Table I of Ref. 15 shows that the inferred compressions from the two analyses are almost identical (as expected). The average relative deviations of u_2 and η_2 are 0.2% and 0.5%, respectively for the first seven experiments listed in Table VI. For flyer-plate experiments with low-impedance samples, the off-Hugoniot uncertainty ($\partial u_2 / \partial \epsilon$) dominates the systematic error; the Hugoniot uncertainty ($\partial u_2 / \partial \lambda$) is ~25 times smaller (also as demonstrated in Fig. 3). As discussed in Sec. III C 2, this demonstrates an advantage of the flyer-plate technique for this kind of experiment, because the impedance-match analysis is insensitive to inaccuracies in the principal Hugoniot of the model used in the analysis. From our impedance-match analysis the magnitude of the systematic uncertainty is ~4% in the compression (~8% at 2σ confidence), which is consistent with the estimates of Knudson *et al.* This uncertainty

is directly traceable to theoretical and experimental uncertainties in the release profile pressure correction, as discussed previously in Sec. IV B 2.

The impedance-match analysis of the last experiment, Z946, appears to be an outlier. Compared to the other experiments the analysis result deviates by 0.7% in u_2 and 2.3% in η_2 from the analysis with the 3700 EOS. Since the Hugoniot uncertainty plays no role here, this discrepancy must originate from a difference between the release profile predicted by 3700 compared with that predicted by our model-averaged correction. The 2.3% discrepancy is well within our estimated 4% uncertainty, thus there is no reason to favor one result over the other. No release profile data is currently available to test the models at these conditions.

The random uncertainty for individual shots is about 10%, roughly 2.5 times larger than the systematic error. The random uncertainties can be reduced by averaging, which was done by Knudson *et al.* for several of their measurement points. It is interesting to note that the measurement uncertainty in these experiments is dominated by the measurement of the flyer-plate velocity: The $\partial u_2 / \partial \xi$ contribution overwhelms the $\partial u_2 / \partial \zeta$ contribution by a factor of 7–25.

D. High-pressure EOS of deuterium, incident shock method

U_1-type impedance-match EOS measurements on solid deuterium driven by a convergent explosive system have been reported by Belov *et al.*[16] and Boriskov *et al.*[17] More recently similar measurements on liquid deuterium have been reported by Boriskov *et al.*;[18] however, in the latter report the authors listed only the analyzed $U_2 - u_2$ values and did not give the underlying U_1 data, thus it is not possible to assess the systematics of the latter study. In Table VII we show an analysis of Belov *et al.*[16] and Boriskov *et al.*[17] for the purpose of comparing the systematic errors with the u_1-type measurements of Knudson *et al.*.

The compression results produced by our analysis in Table VII are approximately 3.3% higher than found in Ref. 16 and 1.0% higher than in Ref. 17; thus our impedance-match model appears to be slightly softer than that used by

TABLE VII. Analysis of U_1-type impedance-match data for D_2 from Belov *et al.* (Ref. 16) and Boriskov *et al.* (Ref. 17).

Expt.	ρ_{10}	ρ_{20}	$U_1(\delta U_1)$	$U_2(\delta U_2)$	$\frac{\partial u_2}{\partial \xi}$	$\frac{\partial u_2}{\partial \zeta}$	$\frac{\partial u_2}{\partial \lambda}$	$\frac{\partial u_2}{\partial \epsilon}$	$u_2(\text{ran},\text{sys})$ (km/s)	$P_2(\text{ran},\text{sys})$ (GPa)	$\eta_2(\text{ran},\text{sys})$
	(g cm^{-3})		(km/s)		(km/s$\times 10^{-3}$)						
Ref. 16	2.74	0.199	16.39(10)	20.30(20)	157	−19	−127	197	14.90(16,23)	60.20(82,95)	3.76(16,16)
Ref. 17	2.74	0.199	21.20(30)	28.20(60)	476	−64	−158	243	21.70(48,29)	121.8(3.5,1.6)	4.34(47,19)

those authors. However, these discrepancies are within the estimated range of systematic uncertainty, which is ∼4.3% for the conditions of those experiments. One may assume that a similar level of 4%–5% systematic uncertainty applies to the analysis in.[18]

For the experiments listed in Table VII the release profile uncertainty contribution ($\partial u_2 / \partial \epsilon$) is larger than the Hugoniot uncertainty contribution ($\partial u_2 / \partial \lambda$), and in comparison with Table VI the systematic uncertainties for the U_1-type measurements are only somewhat larger (about 20%) than for the u_1-type measurements. This is because both methods are equally affected by the dominant release profile uncertainty.

VI. DISCUSSION

We have presented an accurate method of performing ultrahigh-pressure impedance-match analysis for two common types of impedance-match experiments. The impedance-match EOS for the Al shock-wave standard, including uncertainties, is described completely by Tables II and III in conjunction with Eqs. (14)–(19). The Al fit is somewhat softer than existing tabular models and will produce softer results for most impedance-match data. The analysis method amounts to finding a root of a polynomial of quadratic or cubic order and is summarized in Eqs. (20)–(27). The systematic uncertainties estimated by the analysis method are directly traceable to the uncertainties in the fit to the absolute Hugoniot data and to the standard deviation of the pressure corrections predicted by an ensemble of theoretical models. As the data for the Al principal Hugoniot and improved theoretical models become available, the information can be incorporated easily into the analytical forms developed here, in order to improve the analysis of current and future experiments.

A potential weakness of the current analysis is the fact that the theoretical estimates for the pressure corrections are largely unconstrained by the data for both reshock and release states at high pressures (>1 TPa); the pressure corrections under these conditions are therefore almost entirely model dependent. Since the pressure corrections are increasing in the limit of extreme pressures, it seems important to produce experimental data that test the theoretical predictions for Al (and other standards) under strong reshock and release at pressures >1 TPa.

APPENDIX

1. Linear and quadratic fittings to the principal Hugoniot

The fits used in this study are all derived using least-squares fitting of a primary data set over an orthogonal polynomial basis. The form of the fit used is

$$U = a_0 X_0 + a_1 X_1 + a_2 X_2, \tag{A1}$$

where the basis is defined by a constant term $X_0 = 1$, a first-order polynomial $X_1 = (u - \beta)$, and a quadratic polynomial $X_2 = (u - \gamma_1)(u - \gamma_2)$. The coefficients of the fit, a_i, are determined from a weighted χ^2 minimization of the polynomial form above relative to the measured data set. The data set is comprised of measurement pairs $(u_i \pm \delta u_i, U_i \pm \delta U_i)$, where δu_i and δU_i are the individual measurement errors of u_i and U_i, respectively. For fitting the u_i are regarded as independent, and the U_i are dependent with standard deviation $\sigma_i^2 = \delta U_i^2 + 1.26^2 \delta u_i^2$ assigned to each datum; the δu_i contribution to σ_i is weighted by the 1.26^2 factor to account approximately for the average slope ($s \simeq 1.26$ for Al) along the principal Hugoniot. The weight assigned to each datum is $w_i = \sigma_i^{-2}$.

The basis used for the fit requires the additional parameters β, γ_1, and γ_2. While these parameters depend on the data set, their dependence is only on the independent variables, u_i, and not on the measured variables, U_i. Errors are not assigned to β, γ_1, and γ_2, and they are calculated and maintained to a high precision. The orthogonal basis is determined by the expressions defined below, which were derived following a procedure outlined by Bevington.[47] Initially, we compute several weighted sums,

$$W = \sum_{i=1}^{N} w_i, \quad \Sigma_u = \sum_{i=1}^{N} w_i u_i, \quad \Sigma_{u^2} = \sum_{i=1}^{N} w_i u_i^2, \tag{A2}$$

$$\Sigma_{u^3} = \sum_{i=1}^{N} w_i u_i^3,$$

where the summations are made over N data points. These terms are combined to define the parameters of the orthogonal polynomial basis up to second order,

$$\beta = \Sigma_u / W,$$

$$\gamma_1 = \frac{\Sigma_u \Sigma_{u^2} - W\Sigma_{u^3} - \sqrt{(\Sigma_u \Sigma_{u^2} - W\Sigma_{u^3})^2 + 4(\Sigma_u^2 - W\Sigma_{u^2})(-\Sigma_{u^2}^2 + \Sigma_u \Sigma_{u^3})}}{2(\Sigma_u^2 - W\Sigma_{u^2})},$$

$$\gamma_2 = \frac{\Sigma_u \Sigma_{u^2} - W\Sigma_{u^3} + \sqrt{(\Sigma_u \Sigma_{u^2} - W\Sigma_{u^3})^2 + 4(\Sigma_u^2 - W\Sigma_{u^2})(-\Sigma_{u^2}^2 + \Sigma_u \Sigma_{u^3})}}{2(\Sigma_u^2 - W\Sigma_{u^2})}.$$

Using the above definitions it can be shown that the basis has the property

$$\sum_{i=1}^{N} w_i X_j(u_i) X_k(u_i) = 0 \quad \text{for } j \neq k, \tag{A3}$$

which is the orthogonality condition.

The weighted least-squares fit of the data (χ^2 minimization) is given by solving a system of $n+1$ equations for an n-order fit for the coefficients a_j. The equations can be represented in matrix form as

$$z_k = a_j \alpha_{jk} \quad \text{for } k = 0, \ldots, n, \tag{A4}$$

where

$$z_k = \sum_{i=1}^{N} w_i U_i X_k(u_i) \text{ and } \alpha_{jk} = \sum_{i=1}^{N} w_i X_j(u_i) X_k(u_i). \tag{A5}$$

The matrix $\boldsymbol{\alpha}$ is diagonal (i.e., $\alpha_{jk} = 0$ for $j \neq k$) because of the orthogonality condition of Eq. (A3). The inverse, $\boldsymbol{\epsilon} = \boldsymbol{\alpha}^{-1}$, is needed to solve the matrix equations and to evaluate the errors in the coefficients; $\boldsymbol{\epsilon}$ is also diagonal. The standard deviations for the uncertainties in the fit coefficients are given by

$$\sigma_{a_j}^2 = \sum_{i=1}^{N} \left[\sigma_i^2 \left(\frac{\partial a_j}{\partial U_i} \right)^2 \right]. \tag{A6}$$

However, from the fact that the matrices are diagonal,

$$\left(\frac{\partial a_j}{\partial U_i} \right) = \sum_{j=0}^{n} \epsilon_{jk} w_i X_k(u_i) = \epsilon_{jj} w_i X_j(u_i), \tag{A7}$$

which leads to the following expression for the uncertainties:

$$\sigma_{a_j}^2 = \epsilon_{jj}^2 \sum_{i=1}^{N} w_i X_j(u_i)^2. \tag{A8}$$

Because the matrices have zero-valued off-diagonal elements, the covariance among the fitting coefficients vanishes, and the error contributions can be propagated using simple quadrature combinations of the individual contributions as indicated in Eq. (15).

2. Determining the off-Hugoniot pressure correction

The off-Hugoniot corrections are determined entirely from theoretical EOS models for the reference standard as follows. For each model m we begin by computing the prin-

cipal Hugoniot predicted by the model, $P_{Hm}(u)$, and then choose a series of states j, parameterized by particle velocity u_j along the principal Hugoniot (giving model-dependent U_{jm}). Starting from these states we compute the second shock Hugoniot $P_{\text{rsk}_{jm}}(u)$ and release profiles $P_{\text{rel}_{jm}}(u)$, centered on the Hugoniot state j. Finally, from each of these calculated profiles, we subtract the approximate profile represented by the mirror-reflected Hugoniot $P_{M_{jm}}(u) = P_{H_m}(2u_{jm} - u)$, centered at the state j,

$$P_{C_{jm}}(u) = \begin{cases} P_{\text{rsk}_{jm}}(u) - P_{H_m}(2u_{jm} - u), & u < u_{jm} \\ P_{\text{rel}_{jm}}(u) - P_{H_m}(2u_{jm} - u), & u \geq_{jm}. \end{cases} \tag{A9}$$

Therefore, the $P_{C_{jm}}(u)$ represent a pressure correction that must be added to the mirror-reflected Hugoniot of state j in order to retrieve the exact reshock and release profiles for that model. By compiling a series of such correction curves over a range of states j, one may generate the correction over a wide range of parameter space by interpolation methods.

This construction is designed to normalize a given theoretical EOS model against a measured Hugoniot, yet retain the information in the model pertaining specifically to the off-Hugoniot states. That is, starting from a measured Hugoniot $P_{H_{\text{fit}}}(u)$, one can define a $P_{M_{j\text{fit}}}(u)$ for state j and combine it with the correction $P_{C_{jm}}(u)$ for state j of model m, in order to generate an impedance-match EOS that incorporates accurately both the *measured principal Hugoniot* and the *theoretical off-Hugoniot physics* represented in model m. It turns out that the theoretical picture is uncertain because different models produce different estimates for $P_{C_j}(u)$; therefore, we estimate a model-dependent uncertainty $\sigma_{P_{C_j}}(u)$ based on the variation among models. The discussion below presents a compact polynomial construction for representing this model-dependent information including the estimate of the model-dependent uncertainty. The procedures outlined in Sec. III C provide the means for incorporating $\sigma_{P_{C_j}}(u)$ into the impedance-match analysis.

To generate the polynomial fits we define a normalized pressure correction,

$$p_{n_{jm}}(q) = P_{C_{jm}}[(q + 1)u_j]/P_{H_m}(u_j). \tag{A10}$$

Here, $P_{C_{jm}}(u)$ is scaled by the Hugoniot pressure of the incident state and mapped onto a normalized velocity coordinate, $q = u/u_j - 1$, with origin $q = 0$ centered on the incident shock state u_j. The goal of the fit is to approximate $p_{n_{jm}}(q)$ accu-
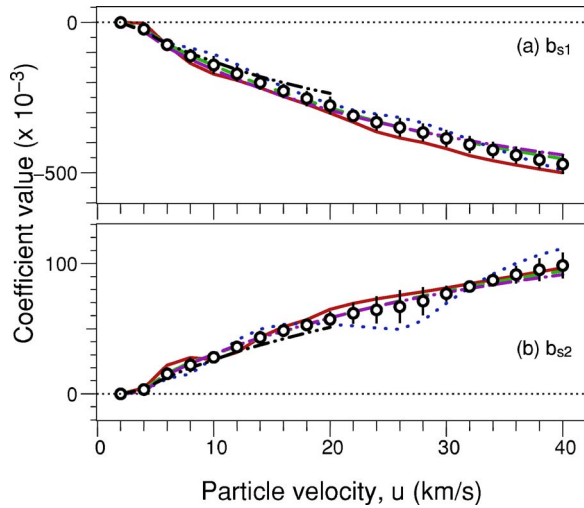
FIG. 11. (Color online) Open circles show the model-averaged reshock branch pressure correction coefficients (a) b_{s1} and (b) b_{s2}; the corresponding error bars show the magnitudes of (a) $\sigma_{b_{s1}}$ and (b) $\sigma_{b_{s2}}$. Also shown are the coefficient values determined from the underlying models: SESAME 3715 (solid, red), SESAME 3719 (dash, green), SESAME 3713 (dotted, blue), QEOS (chain-dot, magenta), and 3700 (chain-dot-dot, black) (Ref. 40).

rately [$\sim 1\%$ of $P_{H_m}(u_j)$] with a small number of coefficients. In general the normalized reshock pressure correction $P_{\mathrm{rsk}_{jm}}(q)$ can be fitted to this accuracy by a quadratic polynomial in q and the release branch, $P_{\mathrm{rel}_{jm}}(q)$ by a cubic polynomial in q. We choose the Chebyshev polynomials to construct the fits to the $p_{n_{jm}}$ because of their orthogonality and near-optimal minimization of errors over a finite fitting domain.

Practical limits for the appropriate ranges of q depend on the limiting impedances of possible samples. Release of Al into cryogenic liquid H_2 produces values of q ranging from 0.84 to 1.0 for incident shocks in Al from 4 to 0.1 TPa (0.66–0.96 for the case of liquid D_2). At the opposite end of the impedance spectrum estimated reshock conditions in Al for a selection of typical high-impedance samples (e.g., Au and W) show that $-0.6 < q$ in all cases. Intermediate cases are $0.25 < q < 0.42$ for water and $-0.32 < q < -0.25$ for Fe. Therefore, for the purpose of constructing fits to the pressure correction curves, it is sufficient to fit $p_{n_{jm}}(q)$ to the interval $-2/3 < q < 0$ on the reshock branch and to $0 < q < 1$ on the release branch.

The Chebyshev approximation is defined to fit a function over a normalized interval, $-1 < y < 1$; therefore, we define additional mappings according to the two branches,

$$q_s(y) = (y - 1)/3, \tag{A11}$$

$$q_r(y) = (y + 1)/2, \tag{A12}$$

which maps the interval $-1 < y < 1$ to $-2/3 < q_s < 0$ and to $0 < q_r < 1$ for the reshock and release branches, respectively. The Chebyshev coefficient for model m, shock state j, branch t, and order i is then defined by computing the sum,[48]
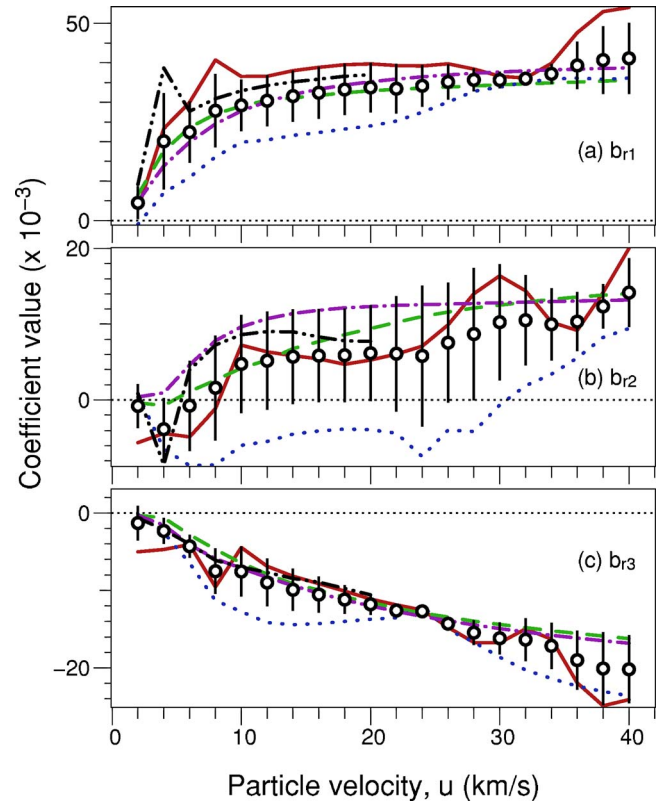

FIG. 12. (Color online) Same as for Fig. 11 for the coefficients of the release branch of the pressure correction.

$$b_{jmti} = \frac{2}{L} \sum_{l=1}^{L} p_{n_{jm}} \left(q_t \left\{ \cos \left[\frac{\pi(l - 1/2)}{L} \right] \right\} \right)$$
$$\times \cos \left[\frac{\pi(l - 1/2)i}{L} \right], \tag{A13}$$

where L is typically a large number (50 in our case, in order to sample the function adequately) and t is either s or r for the shock and release branch mappings, respectively. A separate fit is applied to each case j, and the resulting set of coefficients is tabulated to represent the pressure corrections for a given EOS model over a wide range of states. For the reshock branch we compute coefficients up to $i = 2$ and for release branch up to $i = 3$.

Using these definitions the approximation to $p_{n_{jm}}$ is given by[48]

$$p_{n_{jm}}(q)$$
$$= \begin{cases} \dfrac{-b_{jms0}}{2} + \displaystyle\sum_{i=0}^{2} b_{jmsi} T_i(3q + 1) & \text{for } -2/3 < q \leq 0 \\[4mm] \dfrac{-b_{jmr0}}{2} + \displaystyle\sum_{i=0}^{3} b_{jmri} T_i(2q - 1) & \text{for } 0 < q \leq 1. \end{cases}$$
$$\tag{A14}$$

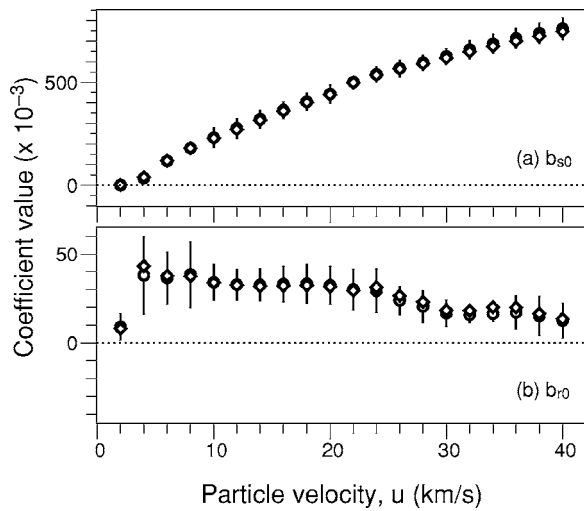Averaging over a set of M models is achieved by averaging the coefficients,

FIG. 13. Open circles show the model-averaged zero-order coefficients (a) b_{s0} and (b) b_{r0} of the (unconstrained) fits to the models; the error bars show the respective standard deviations. The open diamonds show the values of the zero-order coefficient as determined by the constraint equations (A17) and (A18).

$$\langle b_{jti}\rangle = \frac{1}{M}\sum_{m=1}^{M} b_{jmti}. \tag{A15}$$

Uncertainties $\sigma_{b_{jti}}$ are determined from the corresponding standard deviations:

$$\sigma_{b_{jti}} = \left[\frac{1}{M-1}\sum_{m=1}^{M}(b_{jmti}-\langle b_{jti}\rangle)^2\right]^{1/2}. \tag{A16}$$

For a particular experiment characterized by incident shock velocity u_1, we interpolate (linear interpolation is adequate) into the set of $\langle b_{jti}\rangle$ and σ_{jti} that are tabulated against the particle velocities u_j; the interpolated values are referred to as $b_{ti}(u_1)$ and $\sigma_{b_{ti}}(u_1)$ in Eqs. (17) and (18), respectively, with t denoting the branch s or r depending on q. The tabulation for Al is given in Table III.

The coefficients b_{r0} and b_{s0} are not listed in Table III; instead, they are discarded and replaced with an additional constraint to enforce the condition $p_{n_1}(q)\to 0$ as $q\to 0$. This is equivalent to zeroing the constant term in a Taylor series representation of $p_{n_1}(q)$ expanded about $q=0$ [as in Eq. (33)]. The exact corrections $p_{njm}(q)$ of Eq. (A10) have this property while the approximate fits do not. Therefore, the fits are modified by redefining b_{s0} and b_{r0} to satisfy this constraint,

$$b_{s0}(u_1) = -2[b_{s1}(u_1)+b_{s2}(u_1)], \tag{A17}$$

$$b_{r0}(u_1) = 2[b_{r1}(u_1)-b_{r2}(u_1)+b_{r3}(u_1)]. \tag{A18}$$

These constraints are included implicitly in Eqs. (17) and (18) [compare with Eq. (A14)].

The two figures, Figs. 11 and 12, show the values of the reshock and release coefficients, respectively, as fitted to the five models used to construct the averaged correction. Also plotted are the model-averaged values $\langle b_{si}\rangle$ and $\langle b_{ri}\rangle$ with error bars that represent the variation among the models, $\sigma_{b_{si}}$ and $\sigma_{b_{ri}}$, respectively. These plots reveal that the magnitudes of all the correction coefficients are effectively zero in the

limit of weak shocks $u\lesssim 4$ km/s, indicating that the mirror-reflection approximation is very accurate for weak shocks; this fact is well known and consistent with, for example, the velocity doubling rule to estimate the particle velocity in a weak shock from a measurement of the free-surface velocity. On the other hand all of the correction coefficients increase in magnitude for increasing shock strength. In the strong shock domain ($u>6$ km/s) the mirror-reflection approximation will produce increasingly inaccurate results, especially for reshock-type experiments.

In Fig. 13 we compare the values of $\langle b_{s0}\rangle$ and $\langle b_{r0}\rangle$ as determined from the unconstrained Chebyshev fit along with the corresponding values determined from the constraint equations [(A17) and (A18)]. It is evident that the values determined from the constraints are very close to those determined from the unconstrained fits, well within the model-to-model uncertainties; therefore, the imposition of the constraints does not degrade the character or quality of the fit.

[1] J. M. Walsh, M. H. Rice, R. G. McQueen, and F. L. Yarger, Phys. Rev. **108**, 196 (1957).
[2] L. V. Al'tshuler, K. K. Krupnikov, and M. I. Brazhnik, Sov. Phys. JETP **34**, 614 (1958).
[3] Y. B. Zel'dovich and Y. P. Raizer, *Physics of Shock Waves and High-Temperature Hydrodynamic Phenomena* (Academic, New York, 1967), Vol. II.
[4] R. F. Trunin, *Shock Compression of Condensed Materials* (Cambridge University Press, Cambridge, 1998).
[5] W. J. Nellis and A. C. Mitchell, J. Chem. Phys. **73**, 6137 (1980).
[6] W. J. Nellis, F. H. Ree, M. van Thiel, and A. C. Mitchell, J. Chem. Phys. **75**, 3055 (1981).
[7] W. J. Nellis, N. C. Holmes, A. C. Mitchell, D. C. Hamilton, and M. Nicol, J. Chem. Phys. **107**, 9096 (1997).
[8] P. M. Celliers *et al.*, Phys. Plasmas **11**, L41 (2004).
[9] C. E. Ragan III, Phys. Rev. A **25**, 3360 (1982).
[10] C. E. Ragan III, Phys. Rev. A **29**, 1391 (1984).
[11] A. C. Mitchell, W. J. Nellis, J. A. Moriarty, R. A. Heinle, N. C. Holmes, R. E. Tipton, and G. W. Repp, J. Appl. Phys. **69**, 2981 (1991).
[12] M. Koenig *et al.*, Phys. Rev. Lett. **74**, 2260 (1995).
[13] S. D. Rothman, A. M. Evans, C. J. Horsfield, P. Graham, and B. R. Thomas, Phys. Plasmas **9**, 1721 (2002).
[14] D. G. Hicks, P. M. Celliers, G. W. Collins, J. H. Eggert, and S. J. Moon, Phys. Rev. Lett. **91**, 035502/1–4 (2003).
[15] M. D. Knudson, D. L. Hanson, J. E. Bailey, C. A. Hall, J. R. Asay, and C. Deeney, Phys. Rev. B **69**, 144209 (2004).
[16] S. I. Belov *et al.*, JETP Lett. **76**, 433 (2002).
[17] G. V. Boriskov *et al.*, Dokl. Phys. **48**, 553 (2003).
[18] G. V. Boriskov *et al.*, Phys. Rev. B **71**, 092104 (2004).
[19] B. S. Chekin, J. Appl. Mech. Tech. Phys. **19**, 212 (1978).
[20] M. V. Zhernokletov, G. V. Simakov, Y. N. Sutulov, and R. F. Trunin, High Temp. **33**, 36 (1995).
[21] M. D. Knudson, J. R. Asay, and C. Deeney, J. Appl. Phys. **97**, 073514 (2005).
[22] V. A. Bugaeva, A. A. Evstigneev, and R. F. Trunin, High Temp. **34**, 674 (1995).
[23] R. G. McQueen, S. P. Marsh, J. W. Taylor, J. N. Fritz, and W. J. Carter, *High-Velocity Impact Phenomena* (Academic, New York, 1970), Chap. VII, pp. 294–417.
[24] W. J. Nellis, H. B. Radousky, D. C. Hamilton, A. C. Mitchell, N. C. Holmes, K. B. Christianson, and M. van Thiel, J. Chem. Phys. **94**, 2244 (1991).
[25] J. D. Johnson, in *Shock Compression of Condensed Matter–1997*, edited by S. Schmidt, D. P. Dandekar, and J. W. Forbes (AIP, New York, 1998), pp. 27–30.
[26] See National Technical Information Service Document No. DE94-011699. (J. D. Johnson, Los Alamos National Laboratory Report No. LA-UR-94-1451, 1994). Copies may be ordered from the National Technical Information Service, Springfield, VA.
[27] A. C. Mitchell and W. J. Nellis, J. Appl. Phys. **52**, 3363 (1981).

[28]To third order the Chebyshev polynomials are $T_0(x)=1$, $T_1(x)=x$, $T_2(x)=2x^2-1$, and $T_3(x)=4x^3-3x$.

[29]L. V. Al'tshuler, S. B. Kormer, A. A. Bakanova, and R. F. Trunin, Sov. Phys. JETP **11**, 573 (1960).

[30]M. D. Knudson, R. W. Lemke, D. B. Hayes, C. A. Hall, C. Deeney, and J. R. Asay, J. Appl. Phys. **94**, 4420 (2003).

[31]M. D. Knudson, J. Appl. Phys. (to be published). These data include nine data points from 600 to 1200 GPa. Techniques used were similar to those reported in Ref. 30. The data are included in determining the fit coefficients in Table II; however, they are not included in Table I nor in Fig. 4.

[32]V. Simonenko, N. P. Voloshin, A. S. Vladimirov, A. P. Nagibin, V. N. Nogin, V. A. Popov, V. A. Vasilenko, and Y. A. Shoidin, Sov. Phys. JETP **61**, 869 (1985).

[33]A. P. Volkov, N. P. Voloshin, A. S. Vladimirov, V. N. Nogin, and V. A. Simonenko, JETP Lett. **31**, 588 (1980).

[34]M. A. Podurets, V. M. Ktitorov, R. F. Trunin, L. V. Popov, A. Y. Matveev, B. V. Pechenkin, and A. G. Sevast'yanov, High Temp. **32**, 890 (1994).

[35]G. I. Kerley, Int. J. Impact Eng. **5**, 441 (1987).

[36]The Al EOS developed by Kerley (Ref. 35) is used at the Sandia National Laboratories and commonly referred to as the 3700 table.

[37]R. F. Trunin, M. A. Podurets, G. V. Simakov, L. V. Popov, and A. G. Sevast'yanov, JETP **81**, 464 (1995).

[38]R. F. Trunin, L. F. Gudarenko, M. V. Zhernokletov, and G. V. Simakov, *Experimental Data on Shock Compression and Adiabatic Expansion of Condensed Matter* (RFNC-VNIIEF, Sarov, 2001).

[39]R. M. More, K. H. Warren, D. A. Young, and G. B. Zimmerman, Phys. Fluids **31**, 3059 (1988).

[40]P. R. Bevington, *Data Reduction and Error Analysis for the Physical Sciences* (McGraw-Hill, New York, 1969), Chap. 9, p. 96.

[41]The pressure corrections include the 3700 table only to $u_1=20$ km/s, because pressures above this extend beyond the upper limit of this table. Above this limit the coefficients represent an average over the four remaining models.

[42]W. J. Nellis, A. C. Mitchell, and D. A. Young, J. Appl. Phys. **93**, 304 (2003).

[43]N. C. Holmes, in *High Pressure Science and Technology–1993*, edited by S. Schmidt, J. Shaner, and G. Samara (AIP, New York, 1994), pp. 153–156.

[44]R. G. McQueen, J. N. Fritz, and C. E. Morris, in *Shock Waves in Condensed Matter–1983*, edited by J. R. Asay, R. A. Graham, and G. K. Straub (Elsevier, Amsterdam, 1984), pp. 95–98.

[45]T. Neal, Phys. Rev. B **14**, 5172 (1976).

[46]R. S. Hixson and J. N. Fritz, J. Appl. Phys. **71**, 1721 (1992).

[47]P. R. Bevington, *Data Reduction and Error Analysis for the Physical Sciences* (McGraw-Hill, New York, 1969), Chap. 8, pp. 134–63.

[48]W. H. Press, B. P. Flannery, S. A. Teukolsky, and W. T. Vetterling, *Numerical Recipes* (Cambridge University Press, Cambridge, 1986), Chap. 5, pp. 147–51, we use a slightly different notation by indexing the coefficients beginning at 0 rather than 1.

[49]L. V. Al'tshuler, A. A. Bakanova, and R. F. Trunin, Sov. Phys. JETP **15**, 65 (1962).

[50]S. B. Kormer, A. I. Funtikov, V. D. Urlin, and A. N. Kolesnikova, Sov. Phys. JETP **15**, 477 (1962).

[51]C. E. Ragan III, M. G. Silbert, and B. C. Diven, J. Appl. Phys. **48**, 2860 (1977).